



HAL
open science

Dynamic modeling and simulation of a concentrating solar power plant integrated with a thermochemical energy storage system

Ugo Pelay, Lingai Luo, Yilin Fan, Driss Stitou

► To cite this version:

Ugo Pelay, Lingai Luo, Yilin Fan, Driss Stitou. Dynamic modeling and simulation of a concentrating solar power plant integrated with a thermochemical energy storage system. *Journal of Energy Storage*, 2020, 28, pp.101164. 10.1016/j.est.2019.101164 . hal-02500975

HAL Id: hal-02500975

<https://hal.science/hal-02500975v1>

Submitted on 24 Nov 2020

HAL is a multi-disciplinary open access archive for the deposit and dissemination of scientific research documents, whether they are published or not. The documents may come from teaching and research institutions in France or abroad, or from public or private research centers.

L'archive ouverte pluridisciplinaire **HAL**, est destinée au dépôt et à la diffusion de documents scientifiques de niveau recherche, publiés ou non, émanant des établissements d'enseignement et de recherche français ou étrangers, des laboratoires publics ou privés.

Dynamic Modeling and Simulation of a Concentrating Solar Power Plant Integrated with a Thermochemical Energy Storage System

Ugo PELAY^a, Lingai LUO^{a,*}, Yilin FAN^a, Driss STITOU^b

^a *Université de Nantes, CNRS, Laboratoire de thermique et énergie de Nantes, LTeN, UMR6607, F-44000 Nantes, France*

^b *Laboratoire PROcédés, Matériaux et Energie Solaire (PROMES), CNRS UPR 8521, Tecnosud, Rambla de la Thermodynamique, 66100 Perpignan, France*

Abstract:

This paper presents the dynamic modeling & simulation of a concentrating solar power (CSP) plant integrated with a thermochemical energy storage (TCES) system. The TCES material used is calcium hydroxide and the power cycle studied is a Rankine cycle driven by the CSP. Firstly, dynamics models of components written in Modelica language have been selected, developed, parametrized, connected and regulated to create the CSP plant with different TCES integration concepts. Then simulations were then performed to determine and compare the energy efficiency, water consumption and energy production/consumption of three integrations concepts for two typical days (summer and winter) and for a basic continuous production mode. After that, a feasibility study has been performed to test a peak production scenario of the CSP plant.

The results showed that a TCES integration could increase the overall efficiency of the CSP plant ~~efficiency~~ by more than 10%. The Turbine integration concept has the best global efficiency (31.39% for summer; 31.96% for winter). The global electricity consumption of a CSP plant with TCES represents about 12% of its total energy production for a summer day and 3% for a winter day. An increased nominal power by a factor of 10 could be reached for the peak production mode within one hour using the Turbine integration concept, but with a lower global efficiency (17.89%).

Keywords: Thermal energy storage (TES); Thermochemical energy storage (TCES); Concentrating solar power (CSP); Dynamic modeling; Production mode; Integration concept

Abbreviations

CSP: Concentrated solar power; DNI: Direct normal irradiance; HTF: Heat transfer fluid; Int. concept: Integration concept; MENA: Middle East and North Africa; PID: Proportional integral derivative; SPT: Solar power tower; TCES: Thermochemical energy storage; TES: Thermal energy storage

Declarations of interest: none

* Corresponding author. Tel.: +33 240683167; E-mail address: lingai.luo@univ-nantes.fr

42 **I. Introduction**

43

44 Concentrating solar power (CSP) is expected to play a key role in the future energy transition
45 scenarios towards a more electrified world with low-carbon technologies [IEA, 2018]. Meanwhile,
46 thermal energy storage (TES) systems become indispensable to increase the dispatchability and the
47 economic competitiveness of modern large-scale powerful CSP plants [Alva, 2018; Kuravi, 2013].
48 Currently more than 80% of the CSP plants under construction or planned incorporate TES systems
49 [NREL, 2018; IRENA, 2018].

50

51 Sensible storage using molten salt is the most developed and commonly used TES
52 technology for existing CSP plants because of its simplicity, reliability and cost-effectiveness [Pelay,
53 2017a; b]. However, the salt corrosiveness [Ding, 2019; Walczak 2018; Wang, 2019], the limited
54 working temperature [Gimenez, 2015; Villada, 2018] and the risk of salt solidification [Vignarooban,
55 2015; Villada, 2019] are the major drawbacks remaining to be solved. Other sensible TES systems
56 have then been proposed and studied during the last years, as summarized in recent review papers
57 [Mohan, 2019; Nunes, 2019]. As an alternative, latent heat storage using phase change materials
58 (PCMs) is under intensive investigation, owing to their high density and almost constant phase
59 change temperature during charging or discharging [Lin, 2018; Nazir, 2019]. Special attention has
60 been focused on the improvement of their limited thermal conductivity through encapsulation as
61 well as nanomaterials additives [Qureshi, 2018; Tao, 2018].

62

63 Another trend on the TES systems for CSP plants is the development of thermochemical
64 energy storage (TCES) technology based on reversible endothermic/exothermic chemical reactions
65 involving a large amount of reaction heat. TCES systems become a very attractive option because
66 of their high energy density (up to 10 times greater than latent storage) and the long storage
67 duration at ambient temperature [Prieto, 2016]. Latest advances on the thermochemical materials,
68 reactors and processes are reviewed and summarized in Refs [Liu, 2018; Jarimi, 2019]. Recently,
69 great efforts have also been devoted to investigate the appropriate coupling of the TCES system
70 with the power generating cycle (e.g., Rankine cycle; Brayton cycle, etc.) of the CSP plant [e.g.,
71 Alovio, 2017; Cabeza, 2017; Ortiz, 2017; 2018; 2019; Schmidt, 2017; Pelay, 2019]. This process
72 integration issue plays actually a key role on the adaptation of the TCES technology to the future
73 CSP plants. Particularly in our previous study [Pelay, 2019], three TCES integration concepts using
74 $\text{Ca(OH)}_2/\text{CaO}$ couple have been proposed. Energy and exergy analyses results indicated that
75 compared to a reference plant without storage, the TCES integration could significantly improve
76 the adaptability and dispatchability of the CSP plants with the increased power production [Pelay,
77 2019].

78

79 While most of the earlier studies reported in the literature are focused on conceptual or static
80 analysis, detailed exploration of the TCES process integration issue is still lacking. The dynamic
81 behaviors of CSP plant with TCES integration are of particular importance because this type of
82 installation is inherently subjected to transient boundary conditions such as the varying solar
83 irradiation. Moreover, the dynamic simulations also make it possible to highlight the influences of

84 thermal inertia, which has usually been neglected in the static analysis but plays an important role
85 regarding the real operations of the CSP plant.

86
87 As the following work of our previous study [Pelay, 2019], this paper makes a step forward
88 by presenting the dynamic modeling & simulation of a CSP plant integrated with a TCES system
89 under real conditions. Dynamic models of each component written in the Modelica language have
90 been either adopted from the Dymola library or developed in-house. These models have then been
91 parametrized and further interconnected to build the global model for the CSP plant with TCES
92 integration. The main objectives of this study include: (1) to characterize, *for the first time*, the
93 dynamic behaviors of a CSP plant coupled with a TCES unit; (2) to compare the performances of
94 different TCES integration concepts under realistic variable environmental conditions; (3) to
95 showcase the feasibility of the basic continuous production mode and the peak production mode by
96 implementing advanced control strategies. The contributions of this paper are important because it
97 will expand the limited literature and provide additional insights on the dynamic behaviors of CSP
98 plants with TCES integration. The results obtained may be used for the large deployment of the
99 TCES technology in CSP plants.

100
101 The rest of the paper is organized as follows. Section 2 introduces the methodology used for
102 this study, including the proposed TCES integration concepts, the mathematic model for individual
103 component, the operation mode, the control and the initialization parameters. Section 3 presents
104 and compares the dynamic simulation results for the CSP with different TCES integration concepts
105 under the continuous production mode. Section 4 reports a feasibility study on the peak production
106 mode with the Turbine integration concept. Finally, main findings are summarized in section 5.

109 2. Methodology

110
111 In this section, the three TCES integration concepts previously proposed are briefly
112 introduced. Then the dynamic model for each individual component used in the simulation is
113 presented. The production scenarios, the control strategy, the simulation parameters and the
114 initialization used for this study are also explained.

117 2.1. Proposed TCES integration concepts in a CSP plant

118
119 The reference 100 MW_e CSP plant based on the Solar Power Tower (SPT) technology is
120 schematically shown in Fig. 1. The solar tower group is mainly composed of the tower and the
121 central solar receiver installed at the top. The power cycle in this study is a conventional
122 regenerative Rankine cycle including a steam generator, a turbine, a condenser, an open feedwater
123 heater and pumps. The TES group is not included in this reference SPT plant.

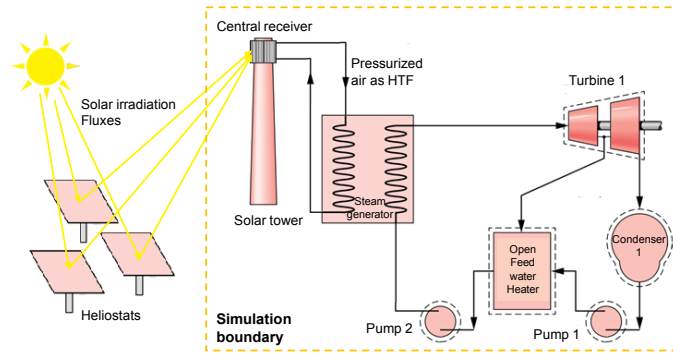
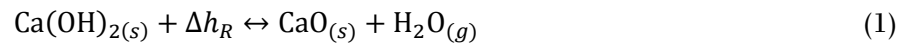


Figure 1. Schematic view of the reference SPT plant without TES. Adapted from [Pelay, 2019]

Different TCES integration concepts have been proposed for ~~a this~~ conceptual ~~Solar Power Tower (SPT) plant~~ [Pelay, 2019]. ~~The TCES reaction couple used is SPT plant using~~ $\text{CaO}/\text{Ca}(\text{OH})_2$ ~~as the reaction couple and the power cycle studied is a Rankine cycle driven by the CSP.~~ The charging stage uses solar energy for the decomposition of $\text{Ca}(\text{OH})_2$ into CaO and the ~~water vapor steam~~ while the discharging stage gets the CaO and the ~~water vapor steam~~ into contact for heat release by the exothermic reaction, as shown by the reaction formula in Eq. (1). For a reaction temperature at $500\text{ }^\circ\text{C}$, the equilibrium pressure equals to 0.1 MPa (1 bar).

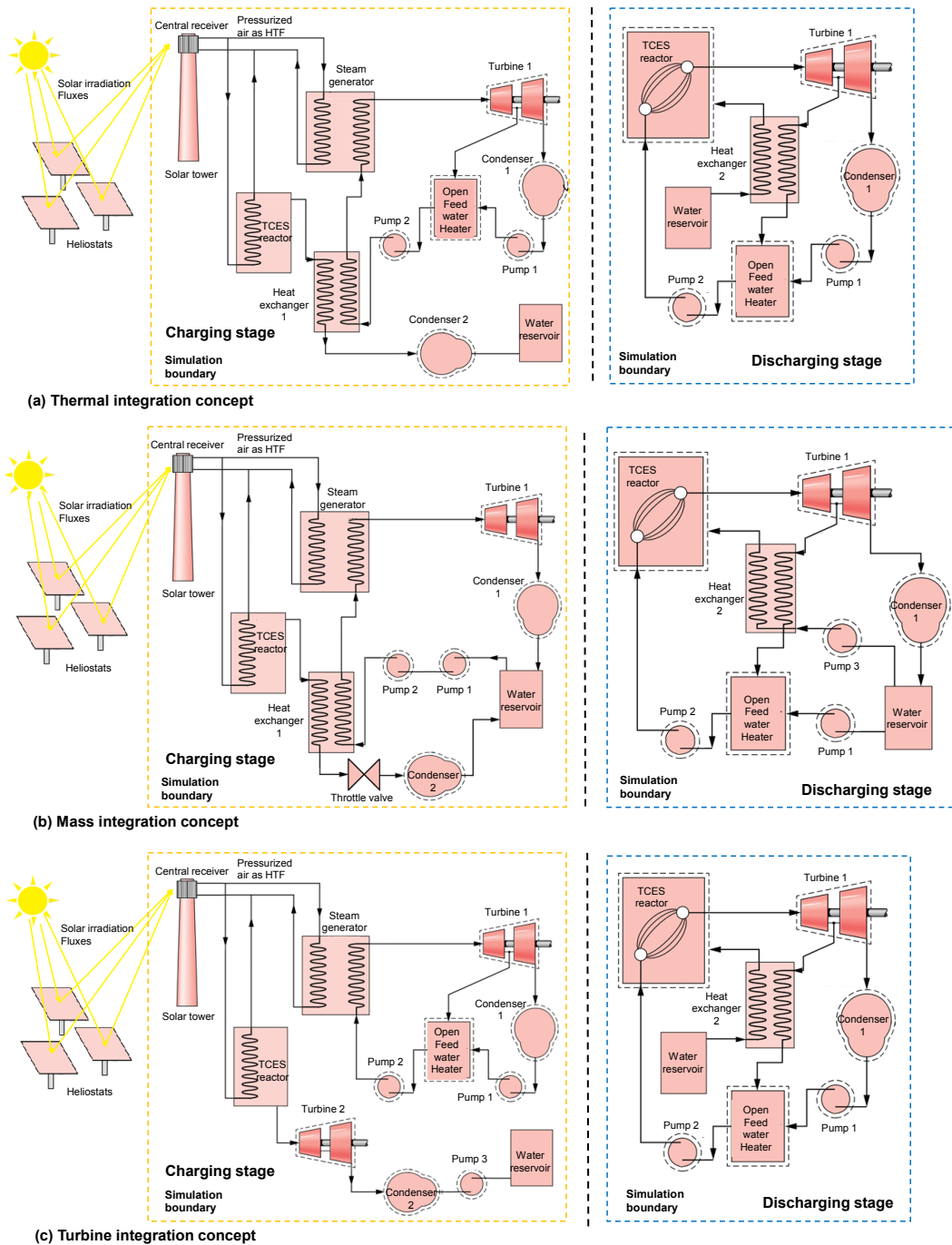


The amount of produced water is preferably to be stored in the liquid form rather than in the ~~gaseous steam~~ form during the period between the charging and discharging, so as to largely reduce the required volume of the storage unit. The proposed TCES integration concepts then distinguish themselves by the management of the ~~water vapor steam~~ from the TCES reactor for energy-efficient coupling between the TCES unit and the Rankine cycle, briefly described as follows.

- *Thermal integration (Thermal Int.)*: during the charging stage, ~~water vapor steam~~ ($500\text{ }^\circ\text{C}$, 1 bar) released from the TCES reactor is partially condensed in a heat exchanger to preheat the working fluid of the Rankine cycle, then completely condensed by a condenser and stored as the saturated liquid ($100\text{ }^\circ\text{C}$, 1 bar) in a separate water reservoir. During the discharging stage, steam extracted from the turbine of the power cycle is used to vaporize the stored liquid water to the saturated vapor ($100\text{ }^\circ\text{C}$, 1 bar), which will then enter into the TCES reactor for exothermic reaction. The Rankine cycle and the TCES circuit are *thermally coupled* with each other but without direct mass contact or exchange (as shown in ~~Fig. 3 of [Pelay, 2019]~~ Fig. 2a).
- *Mass integration (Mass Int.)*: the high temperature ~~water vapor steam~~ generated in the TCES reactor during the charging stage is stored as the saturated water ($41\text{ }^\circ\text{C}$, 0.008 MPa) in a *water reservoir shared with* the Rankine cycle. During the discharging stage, the stored liquid water is firstly pressurized by a pump and then evaporated into saturated vapor ($100\text{ }^\circ\text{C}$, 0.1 MPa) by high temperature extracted steam from the Turbine. For this concept, the Rankine power cycle and the TCES circuit *are coupled and share the same working fluid with mass exchange* (as shown in ~~Fig. 2b-Fig. 4 of [Pelay, 2019]~~).

161
 162
 163
 164
 165
 166
 167
 168
 169
 170

- *Turbine integration (Turbine Int.):* during the charging stage, high temperature ~~water~~ vapor steam (500 °C, 1 bar) from the TCES reactor passes through *an additional turbine* to valorize a part of its thermal energy as power production. The condensed water (41.5 °C, 0.1 MPa) is stored in a separate water reservoir. The discharging stage is the same as that of the Thermal Int. The principal Rankine circuit and the TCES circuit are completely independent of each other during the charging stage (no heat or mass exchange) and thermally coupled during the discharging stage (as shown in [Fig. 2c-Fig. 5](#) of [Pelay, 2019]).



171

172
173
174
175
176
177
178
179
180

Figure 2. Schematic view of the SPT plant with TCES integration. (a) Thermal Int. concept; (b) Mass Int. concept; (c) Turbine Int. concept. Adapted from [Pelay, 2019]

Detailed description of the three proposed Int. concepts as well as their performance modelling based on static energy and exergy analyses can be found in our earlier work [Pelay, 2019].

Table I. Component model of the CSP plant with TCES integration used for the dynamic modeling

Component (Name)	Library/Reference	Modeling assumptions	Features
Steam turbine (SteamTurbine)	ThermoCycle [Quoilin, 2017]	<ul style="list-style-type: none"> - No thermal inertia - Constant isentropic efficiency 	<ul style="list-style-type: none"> - Simple and robust - The Stodola's law with partial arc admission permits the modeling of a gas expansion without sizing the turbine [Altés Buch, 2014]
Open water tank (OpenTank)	ThermoCycle [Quoilin, 2017] A heat exchange port with the outside is added to model the heat loss	<ul style="list-style-type: none"> - Dynamic energy and mass conservation model - Constant outside pressure - Inlet/outlet fluid at liquid state 	<ul style="list-style-type: none"> - Simple and robust - Constant pressure inside the tank
Closed water tank (Tank_PL)	ThermoCycle [Quoilin, 2017]	<ul style="list-style-type: none"> - Dynamic energy and mass conservation model - Constant outside pressure - Saturated outlet fluid - No heat exchange with the outside 	<ul style="list-style-type: none"> - A closed tank with a variable pressure inside - Inlet fluid can be a mixture of liquid and vapor
Pump (Pump)	ThermoCycle [Quoilin, 2017]	<ul style="list-style-type: none"> - Non-dynamic model - No heat loss - No thermal inertia - Constant isentropic and mechanic efficiencies - Inlet/outlet fluid at liquid state 	<ul style="list-style-type: none"> - Simple and robust - Variable rotation speed
Compressor (Compressor)	ThermoCycle [Quoilin, 2017]	<ul style="list-style-type: none"> - Non-dynamic model - No heat loss - No thermal inertia - Constant isentropic and mechanic efficiencies - Inlet fluid at gaseous state 	
Throttle valve (Valve)	ThermoCycle [Quoilin, 2017]	<ul style="list-style-type: none"> - Non-dynamic model - No heat loss - Incompressible fluid - Quadratic pressure loss for turbulent flow 	<ul style="list-style-type: none"> - Non-linear equations generated by quadratic friction coefficient
Linear valve (LinearValve)	Modelica [Altés Buch, 2014]	<ul style="list-style-type: none"> - Non-dynamic model - No heat loss - Incompressible fluid - Linear pressure drop 	<ul style="list-style-type: none"> - Simple and robust - A no-return option for fluid
Three way valve (Three-way valve)	Modelica Buildings library [MBL, 2018]	<ul style="list-style-type: none"> - Non-dynamic model - No heat loss - Linear pressure drop 	<ul style="list-style-type: none"> - Relatively simple control - Presence of a dead volume preventing sudden pressure variations
TCES reactor (Reactor)	In-house Appendix A1	<ul style="list-style-type: none"> - Uniform temperature in the composite - Uniform temperature in the wall - Uniform temperature in the fluid - Entering vapor is instantly at composite temperature 	<ul style="list-style-type: none"> - Sensitive to pressure variations - Complicated to simulate several reactor in parallel
Solar receiver (Solar_Rec)	In-house Appendix A2	<ul style="list-style-type: none"> - No heat loss - No thermal inertia - Gaseous entering fluid - Uniform temperature in the solar receiver 	<ul style="list-style-type: none"> - Constant convective heat transfer coefficient - Dynamic model

Component (Name)	Library/Reference	Modeling assumptions	Features
Condenser (CrossCondenser)	[Altés Buch, 2014]	<ul style="list-style-type: none"> - Constant temperature of cooling fluid - Fluid to be cooled is treated as a mixture of liquid and vapor - No sub-cooling at the outlet of condenser - No heat loss - No inertia - No liquid stored in the condenser 	<ul style="list-style-type: none"> - Variable heat transfer coefficient - Discretized model on cold side - Possibility to be coupled with a tank at the exit of the hot side - Very sensitive to pressure variations
Condenser (Tank_Condenser)	ThermoCycle [Quoilin, 2017] Based on the Tank model, heat transfer between hot and cold fluids is added in the conservation energy equation	<ul style="list-style-type: none"> - Dynamic model - Wall temperature equals to the hot fluid temperature - Uniform temperature of hot fluid - Fixed outlet temperature of cold fluid - No sub-cooling - Compressible hot fluid - No heat loss - Overestimated heat transfer surface area 	<ul style="list-style-type: none"> - Very robust when coupled with a PID system - Condenser with an integrated tank
Evaporator (Simplified_Evaporator)	In-house Appendix A3	<ul style="list-style-type: none"> - Incompressible fluid - No heat loss - Fixed hot fluid outlet temperature 	<ul style="list-style-type: none"> - Extremely robust - Very fast simulations
Evaporator (Tank_Boiler)	ThermoCycle [Quoilin, 2017] Based on the Tank model, heat transfer between hot and cold fluids is added in the conservation energy equation	<ul style="list-style-type: none"> - Dynamic model - Wall temperature equals to the cold fluid temperature - Uniform temperature of cold fluid - Fixed outlet pinch temperature - No over-heating - Compressible cold fluid - No heat loss - Overestimated heat transfer surface area 	<ul style="list-style-type: none"> - Extremely robust
Heat exchanger (Simplified_Heat_Exchanger)	In-house Appendix A4	<ul style="list-style-type: none"> - Incompressible fluid - No heat loss - Fixed pinch temperature 	<ul style="list-style-type: none"> - Extremely robust - Very fast simulations
Heat exchanger (HxIDInc)	ThermoCycle [Quoilin, 2017]	<ul style="list-style-type: none"> - Dynamic model - Uniform velocity on the cross section - Incompressible cold fluid - Negligible longitudinal heat transfer - No heat loss 	<ul style="list-style-type: none"> - Precise discretized model - Very sensitive to pressure variations

185 2.2. Mathematic model for individual component

186

187 Object-oriented Modelica modeling language is used for this study, enabling the description
188 of transient behaviors by models based on differential, algebraic and discrete equations. The
189 conservative equations of heat and mass transfer are firstly formulated for each component of the
190 CSP plant. These mathematic models are then coupled together to represent the whole CSP plant
191 with TCES integration. The resulting system of equations is solved at each time step by the DASSL
192 (Differential Algebraic System Solver) integration algorithm of Dymola solver [Dassault, 2011].
193 Special attention is given to the initialization of simulations for such a complex system with
194 algebraic loops.

195

196 Too complex model for each individual component is difficult to be solved and coupled
197 together while a simpler model ignoring too many details may not be enough precise. A compromise
198 has thus to be reached between the accuracy and the complexity. Moreover, a global view of the
199 CPS plant to be simulated is also indispensable so as to identify the limiting factors (i.e. components
200 having the highest thermal inertia) for reasonable simplifications on less impacting components.

201

202 For most of the components, existing models in the Dymola library or in the literature are
203 adopted, with some necessary modifications. For the key components of the plant (e.g., solar
204 receiver, TCES reactor), their models are developed in house based on the proposed design and sizing.
205 Table 1 recapitulates the mathematical model used for every component, together with the modeling
206 assumptions of each. Note that for turbomachines (turbines, pumps and compressor), constant
207 coefficients (isentropic and volumetric efficiencies) were used, without taking into account the
208 partial load operation curves. Other components were sized for a nominal case covering all the
209 partial load scenarios and/or integrating variable coefficients. Detailed descriptions of the in-house
210 developed models can be found in Appendix A of this paper.

211

212

213 2.3. Operational mode

214

215 Two clear sunny days (one in summer and another in winter) have been selected at eastern
216 Pyrenees (42.497N, 1.959E) where the Themis power plant is located [Larrouturou, 2014] have been
217 selected. The average Direct Normal Irradiance (DNI) curves [PVGIS] during the day are shown on
218 Fig. 13. For the summer day, the sunrise occurs at 5h07 and sunset at 18h37 whereas for the winter
219 day, the sunrise occurs at 7h52 and sunset at 15h52. The solar power P_{sol} ($\text{W}\cdot\text{m}^{-2}$) based on the DNI
220 data is described by Eqs. (2-3) and will be used as inputs for each time step t (s) of the dynamic
221 simulations. Note that the short DNI variation due to clouds has not been taken into account.

222

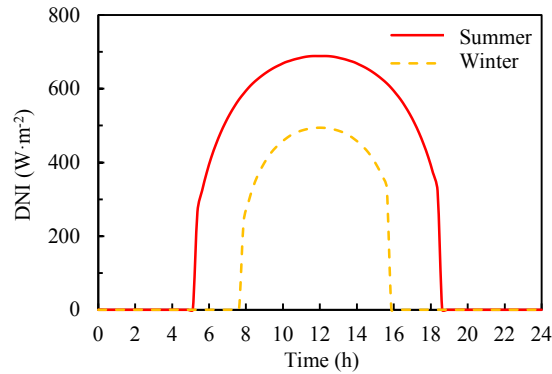
223 For a typical summer day:

$$224 \quad P_{sol} = \begin{cases} \text{if } t \text{ (s)} < 18420; & 0 \\ \text{if } 18420 < t \text{ (s)} < 67020; & -4.985809 \times 10^{-24} \times t^6 + 1.264474 \times 10^{-18} \times t^5 - 1.309668 \times 10^{-13} \times t^4 \\ & + 7.086230 \times 10^{-9} \times t^3 - 2.116637 \times 10^{-4} \times t^2 + 3.328676 \times t - 2.10949 \times 10^4 \\ \text{if } t \text{ (s)} > 67020; & 0 \end{cases} \quad (2)$$

225 For a typical winter day:

$$P_{sol} = \begin{cases} \text{if } t(s) < 28320; & 0 \\ \text{if } 28320 < t(s) < 56220; & -2.86954539 \times 10^{-15} \times t^4 + 4.97529124 \times 10^{-10} \times t^3 - 3.28214478 \times 10^{-5} \times t^2 \\ & + 9.75426171 \times 10^{-1} \times t - 1,05104646 \times 10^4 \\ \text{if } t(s) > 57096; & 0 \end{cases} \quad (3)$$

227



228

229 Figure 4.3. Average DNI for a typical summer and a winter day at eastern Pyrenees (42.497N, 1.959E) [PVGIS]

230

231

232

233

234

235

236

237

The basic production mode is firstly studied for three Int. concepts. The CSP plant is expected to produce electricity continuously at a constant power output over the longest possible period of time with the help of the TCES unit. Nevertheless, the continuous dynamic simulation of the CSP plant for a whole day is difficult at this stage, due to the complicated initialization and calculation instability. As a result, dynamic simulations have been performed for three separate phases of the operational mode, as shown in Fig. 2-4 and explained in detail as follows.

238

239

240

241

242

243

244

245

246

247

248

249

250

251

252

253

254

255

256

257

258

- **Phase 1: plant starting.** At the beginning of a day, the solar power (P_{sol}) is not enough to run the Rankine power cycle at its nominal output ($P_{Rankine}$). This amount of solar energy is used only for the TCES unit, i.e., to preheat the TCES reactor and to initiate the endothermic reaction when the equilibrium reaction temperature (500 °C) is reached.
- **Phase 2: nominal production.** Once the solar power meets the need to run the Rankine power cycle ($P_{sol} > P_{Rankine}$), the nominal production of the CSP plant (phase 2) starts. The TCES system is charged simultaneously by excessive amount of solar energy for later use.
- **Phase 3: prolonged production.** At the end of the day when the decreased solar power becomes insufficient to run the Rankine power cycle at its nominal output ($P_{sol} < P_{Rankine}$), the TCES reactor begins to discharge to compensate the deficiency. The production of CSP plant is prolonged owing to the stored solar energy in phases 1 and 2, until the TCES reactor temperature (T_R) falls below a threshold value fixed by users (e.g., 485 °C). The cut-off temperature of the TCES reactor at the end of phase 3 is determined to equal to 485 °C, permitting still the overheated steam of the principal Rankine cycle at the outlet of the evaporator rising to 480 °C. The heat loss of the TCES reactor overnight is estimated to be negligible supposing that the TCES reactor is well-insulated.

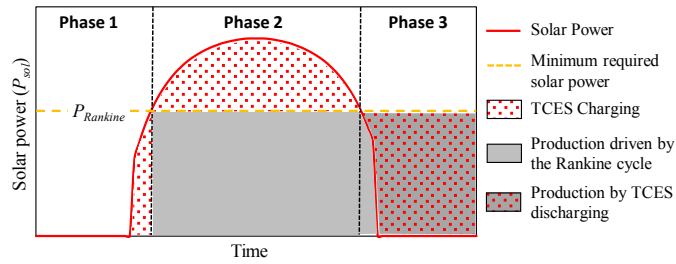


Figure 24. Schematic view of the operational mode divided into 3 phases for the basic continuous production mode

At the end of each phase, all the system's variables (e.g., reactor temperature, ~~receptor~~ solar receiver temperature, pressure in all points, chemical reaction progress) are recorded and transferred to initiate the next phase. Moreover, phase 2 is delayed from the end of phase 1 because discretized components used in the Rankine cycle are unstable to simulate at zero flowrate. Other simulations of the Rankine cycle and more precisely of the evaporator showed that the Rankine cycle needs 15 minute to reach its nominal operation point.

2.4. Control strategy

The proper operation of the CSP plant with TCES integration requires an adapted control strategy to perform multiple controls of the installation. The widely-used PI or PID controllers have been used owing to their robustness and high controlling efficiency. To determine the PID parameters, the manual setup was used whenever possible for simple systems. Otherwise, the Ziegler-Nichols reaction curve method was adopted [Das, 2014]. The controllers used in this study are recapitulated in Table B1 of Appendix B2.

Table 2. List of all PID controllers

Phase	Target	Controlled element	Controller type	Varied parameter
1, 2	HTF's temperature at the outlet of the solar receiver	Compressor rotation speed	PI	Variation of the HTF flowrate
2	Vapor temperature at the outlet of the evaporator	Three way valve opening/closing	PI	Variation of the HTF flowrate passing through the evaporator
3	Vapor temperature at the outlet of the evaporator	Compressor rotation speed	PI	Variation of the HTF flowrate passing through the evaporator
2,3	Pressure at the inlet of the turbine (Rankine cycle)	Turbine's partial arc variation	PI	Variation of the fluid pressure drop in the turbine
1, 2, 3	Pressure of the hot fluid in the condenser	Flow-rate of cooling fluid	PI	Variation of the cooling fluid flow-rate passing through the condenser
3	Pressure of the steam entering into the TCES	Withdrawal valve for the extraction from the turbine	PID	Variation of the withdrawal flow-rate between high pressure and low pressure
2, 3	Tank's water level	Pump's rotation speed	PI	Variation of the water flow-rate outgoing from the tank
2, 3	Fluid temperature at the outlet of the open feedwater heater	Withdrawal valve for the extraction from the turbine	PI	Variation of the withdrawal flow-rate between high pressure and low pressure

2.5. Sizing and simulation parameters

The solar field (heliostats) has been sized so that the TCES reactor can be almost completely charged ($X=0.05$) at the end the charging stage (phase 2) for a summer day. Note that the cosine loss was not considered during the sizing, which may results in an underestimation of the required solar field areas [Peng, 2013]. The solar field surface areas for different TCES integration concepts are listed in Table 23. Details for the modeling of the solar receiver are provided in Appendix A2 of this paper.

Table 23. Sizing of the solar field for different TCES integration concepts

	Thermal Int.	Mass Int.	Turbine Int.
Solar field area (m ²)	1 033 000	1 065 500	908 000

~~The cut-off temperature of the TCES reactor at the end of phase 3 is determined to equal to 485 °C, permitting still the overheated steam of the principal Rankine cycle at the outlet of the evaporator rising to 480 °C. The heat loss of the TCES reactor overnight is estimated to be negligible supposing that the TCES reactor is well insulated.~~

~~The nomenclature, the Pparameter values and variables fixed by the user and controlled by the PID controllers for the dynamic simulation can be found in Tables B2-B5 of Appendix B4-7. Note that the power parasitic consumption is taken into account in the TCES reactor (stoichiometric reaction coefficient) and in the pumps, the turbines and the compressor (isentropic and volumetric efficiency). For other components, no power parasitic consumption is considered.~~

Table 4. Parameter values for different components of the system

	Parameters	Thermal Int.	Mass Int.	Turbine Int.
HTF				
Solar Receiver	Type of fluid	Air	Air	Air
	Masse (kg)	10000	10000	10000
	External surface area (m ²)	1503	1534	1396
	Internal surface area (m ²)	18000	18000	18000
	Heat transfer coefficient (W·K ⁻¹ ·m ²)	150	150	150
Compressor	Isentropic efficiency	0.85	0.85	0.85
	Volumetric efficiency	1	1	1
TCES Reactor				
	Masse of CaO (kg)	1.10×10 ⁷	1.16×10 ⁷	1.11×10 ⁷
	Length/width of CaO plate (m)	6/1	6/1	6/1
	Thickness of CaO plate (mm)	30	30	30
	Thickness of diffuser plate (mm)	5	5	5
	Thickness of wall plate (mm)	2	2	2
	Initial temperature (°C)	495	495	495
	Reaction enthalpy (J·mol ⁻¹)	104000	104000	104000
	Heat capacity ENG (J·K ⁻¹ ·kg ⁻¹)	700	700	700
	Density ENG (kg·m ⁻³)	2250	2250	2250
	Rate of salt (%)	90	90	90
	Kinetic reaction coefficient	5×10 ⁻³	5×10 ⁻³	5×10 ⁻³
	Stoichiometric reaction coefficient	1	1	1
	Convective heat transfer coefficient between wall and reactive salts (W·K ⁻¹ ·m ²)	400	400	400
Turbine 2	Isentropic efficiency	-	-	0.85
	Volumetric efficiency	-	-	1
Pumps	Isentropic efficiency	0.85	0.85	0.85
	Volumetric efficiency	1	1	1

	Parameters	Thermal Int.	Mass Int.	Turbine Int.
Turbine I High Pressure part				
	Isentropic efficiency	0.85	0.85	0.85
	Volumetric efficiency	1	1	1
Turbine I Low pressure part				
	Isentropic efficiency	0.85	0.85	0.85
	Volumetric efficiency	1	1	1
Evaporator				
	HTF outlet temperature (°C)	250	250	250
Condenser				
	Volume (m ³)	100	100	100
	Cold fluid exit temperature (°C)	30	30	30
	Incondensable partial pressure (bar)	0	0	0
Evaporator bleeding				
	Pinch point (°C)	10	10	10
	Incondensable partial pressure (bar)	0	0	0
	Volume (m ³)	10	10	10
Heat exchanger I				
	Pinch point (°C)	10	10	-

310
311
312
313

Table 5. Variables fixed by user - Phase I

	Parameters	Thermal Int.	Mass Int.	Turbine Int.
HTF				
	HTF pressure (bar)	15	15	15
Solar receiver				
	HTF exit temperature (°C)	600	600	600
TCES reactor				
	Steam exit pressure (bar)	1	1	1
Turbine 2				
	Turbine exit pressure (bar)	-	-	0.08

314
315
316
317

Table 6. Variables fixed by user - Phase 2

	Parameters	Thermal Int.	Mass Int.	Turbine Int.
HTF				
	HTF pressure (bar)	15	15	15
Solar Receiver				
	HTF outlet temperature (°C)	600	600	600
TCES Reactor				
	Steam outlet pressure (bar)	1	1	1
Turbine 2				
	Turbine outlet pressure (bar)	-	-	0.08
Pumps				
	Evaporator inlet pressure (bar)	80	80	80
Open feedwater heater				
	Pressure (bar)	8	8	8
	Temperature (°C)	42	42	160
Turbine I High Pressure part				
	Inlet pressure (bar)	80	80	80
	Outlet pressure (bar)	8	8	8
Turbine I Low Pressure part				
	Inlet pressure (bar)	8	8	8
	Outlet pressure (bar)	0.08	0.08	0.08
Evaporator				
	Rankine fluid exit temperature (°C)	480	480	480
Condenser				
	Vapor pressure (bar)	0.08	0.08	0.08
	Liquid level	0.6	0.6	0.6

318
319
320
321

Table 7. Variables fixed by user - Phase 3

	Parameters	Thermal Int.	Mass Int.	Turbine Int.
HTF				
	HTF pressure (bar)	15	15	15
TCES Reactor				
	Steam inlet pressure (bar)	1	1	1
	Steam state	Saturated	Saturated	Saturated
Pumps				
	Evaporator enter pressure (bar)	80	80	80
Open feedwater heater				
	Pressure (bar)	8	8	8
	Temperature (°C)	42	42	160
Turbine I High Pressure Part				
	Inlet pressure (bar)	80	80	80
	Outlet pressure (bar)	8	8	8
Turbine I Low Pressure Part				
	Inlet pressure (bar)	8	8	8
	Outlet pressure (bar)	0.08	0.08	0.08
Evaporator				
	Rankine fluid outlet temperature (°C)	480	480	480
Condenser				
	Vapor pressure (bar)	0.08	0.08	0.08
	Liquid level	0.6	0.6	0.6
	Incondensable partial pressure (bar)	0	0	0
Heat exchanger 2				
	Inside pressure (bar)	1	1	1
	Liquid level	0.6	0.6	0.6

322

323

324 3. Results and discussion for the basic production scenario

325

326 This section shows main results of the dynamic simulation for summer and winter days.
 327 Recall that the solar field and relevant components have been sized to offer an optimal operation
 328 for a typical summer day and for the basic continuous production scenario.

329

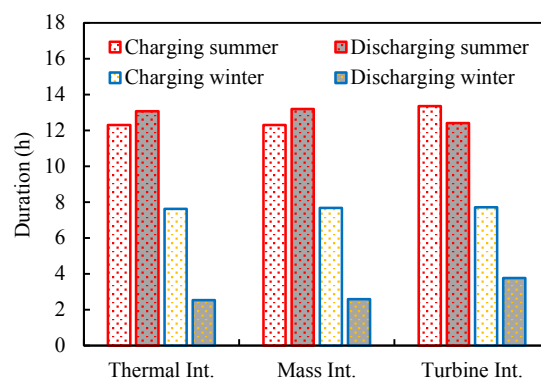
330

331 3.1. Charging/discharging duration

332

333 From Fig. 3-5 one may observe that there is a slight difference on the charging/discharging
 334 durations for different Int. concepts. Indeed, due to their conceptions, all the systems do not need
 335 the same minimal amount of energy to operate. For example, the Turbine Int. concept would benefit
 336 an earlier start and delayed stop, thereby rendering a relatively longer charging and a shorter
 337 discharging in summer. In winter, these durations are significantly lower than those of summer for
 338 all the Int. concepts studied. The CSP plant does not have the necessary solar power to decompose
 339 all the TCES materials: the TCES reactor is largely oversized for a typical "winter" day.

340



341

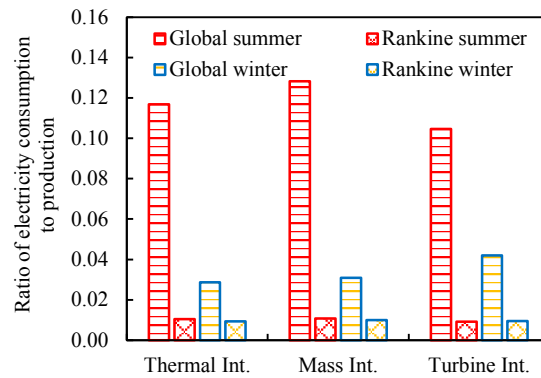
342

Figure 35. Charging/discharging durations for different integration concepts

343
344
345
346
347
348
349
350

3.2. Electricity consumption/production

In order to make an easier comparison between the three integration concepts, the ratios of the electricity consumption (whole plant or Rankine cycle) to the electricity production ~~have been~~ are represented on Fig. 46.



351
352
353
354

Figure 46. Ratio of electricity consumption to production for the CSP plant with different TCES integration concepts ($MW.h_{el\ consumed}/MW.h_{el\ produced}$)

355
356
357
358
359
360
361
362
363
364

The electricity energy is mainly used to run the compressor for the HTF (pressurized air) in the solar circuit and the pumps in the Rankine cycle. In summer, the Rankine cycle electricity consumption is just about one tens of the overall electricity consumption. And in winter, the proportion is one third. It can be noticed from Fig. 4-6 that the electricity consumption for the Rankine cycle is approximately the same for all the integration concepts (about 0.01 $MW.h_{consumed}/MW.h_{produced}$ for both summer and winter). This is because the electricity consumption for running the pumps mainly depends on the mass flow-rate of the Rankine cycle's HTF, which is almost identical for all the integration concepts because of the same nominal production power of 100 MW_{el} .

365
366
367
368
369
370
371
372

The global electricity consumption of the CSP plant is about 12% of the total electricity production for a typical summer day whereas for a typical winter day, the proportion is about 3%. No big difference between the three Int. concepts ~~has been~~ is observed. Meanwhile, the noticeable difference in global consumption between summer and winter is mainly due to the different mass flow-rate of HTF (pressurized air) in the solar circuit. Higher amount of solar energy available in summer needs to be transported by the HTF, resulting in higher electricity consumption in the air compressor.

373
374
375
376
377

Several methods may be employed to decrease the electricity consumption of the compressor (thus the global electricity consumption). A simple way is to raise the upper temperature limit of the HTF (700 °C in the current study) so as to reduce the required HTF mass flow-rate. However, the equipment used for the solar circuit should resist to higher temperature in this case. Another way is to use a liquid HTF having a higher heat capacity (e.g., molten salts, synthetic oils) instead

378 of the pressurized air. But it will bring new problems such as the solidification of molten salts and
 379 the higher environmental impacts [Batuecas, 2017].

380

381

382 3.3. Water consumption

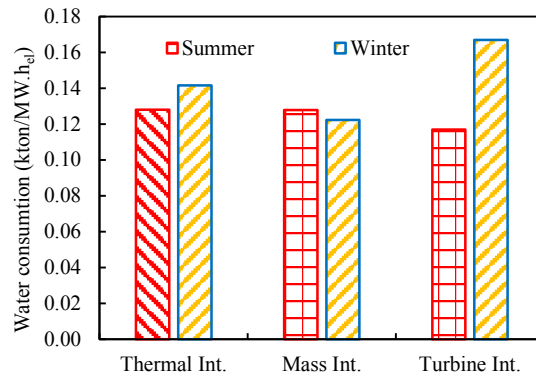
383

384 The water consumption refers to the quantity of cooling water for the condensers of the CSP
 385 plant, one for the Rankine cycle and another for the TCES unit. Note that the cooling water inlet
 386 temperature is 15 °C and the outlet temperature is fixed at 30 °C (maximum allowable temperature
 387 in France) [Khalanski, 1996; MTES, 1998]. Figure 5-7 shows the water consumption (kton) per
 388 MW.h_{el} produced for different Int. concepts of the CSP plant.

389

390 For a typical summer day, the Turbine Int. concept has the lowest water consumption (0.12
 391 kton/MW.h_{el}) because of its highest turbine bleeding at the nominal power that decreases the water
 392 consumption for the condenser of the Rankine cycle. However, for a typical winter day, its water
 393 consumption is the highest (0.17 kton/MW.h_{el}) compared to the Thermal Int concept (0.14
 394 kton/MW.h_{el}) or the Mass Int. concept (0.12 kton/MW.h_{el}). In winter, the ~~charge~~ ~~charging~~ of the
 395 TCES reactor is more important for the Turbine Int. concept, which induces a higher water
 396 consumption. CSP plants are usually installed in desert/remote areas close to the equator (e.g., USA,
 397 Morocco, Spain, MENA [Pelay, 2017a; b]) with summer climate in principle. The Turbine Int.
 398 concept seems to be more beneficial regarding its lower water consumption during summer.

399



400

401 Figure 57. Water consumption (kton/MW.h_{el}) of the CSP plant with different TCES integration
 402 concepts

403

404

405

405 3.4. Energy efficiency

406

407 The Rankine efficiency ($\eta_{Rankine}$) is defined as the efficiency of the Rankine cycle without
 408 considering the solar circuit whereas the global efficiency (η_{Global}) represents the efficiency of the
 409 whole CSP plant. They are calculated following the Eqs. (4) and (5).

$$\eta_{Rankine} = \frac{(W_{T,C} - W_{P,C}) \cdot H_C + (W_{T,D} - W_{P,D}) \cdot H_D}{(Q_{SG} + Q_R) \cdot H_C} \quad (4)$$

$$\eta_{Global} = \frac{(W_{T,C} - W_{P,C} - W_{CP,C}).H_C + (W_{T,D} - W_{P,D} - W_{CP,D}).H_D}{(Q_{SG} + Q_R).H_C} \quad (5)$$

- 410 with: W_T , the energy produced by the turbines (W)
 411 W_P , the energy consumed by the pumps (W)
 412 Q_{SG} , the energy consumed by the Rankine cycle's steam generator (W)
 413 Q_R , the energy consumed by the thermochemical reactor (W)
 414 W_{CP} , the energy consumed by the compressor (W)
 415 H , the duration (h)
 416 The indices C and D indicate the charging and the discharging stage, respectively.
 417

418 Table 3-8 lists the simulated values of global and Rankine energy efficiencies for different
 419 Int. concepts during typical summer and winter days. It can be easily observed that the Turbine
 420 Int. concept has the highest global energy efficiency: 31.39% for summer and 31.96% for winter,
 421 respectively. The option of using a second turbine to valorize the waste heat of high temperature
 422 ~~vapor-steam~~ from the TCES reactor makes it attractive. Despite that the solar field is designed for
 423 summer operation, the winter's global efficiency is higher than that of summer for all the Int.
 424 concepts. In fact, the heat storage in the TCES reactor has two parts: thermochemical reaction heat
 425 and the sensible heat of the reactive salts and the reactor body. The TES by thermochemical
 426 reaction is generally less efficient than the sensible storage due to the heat loss of the superheated
 427 ~~vapor-steam~~ extracted from the TCES reactor during its condensation. For a typical winter day, the
 428 TCES reactor is only partially charged: approximately 20% of the Ca(OH)_2 has been decomposed
 429 whereas it is about 80% for summer. This makes the contribution of the "sensible part" more
 430 important for the total TES, leading to the higher global energy efficiency of the CSP plant. Note
 431 that the reference case (without TES) has a significantly lower global energy efficiency of 21.50%.
 432 Indeed, an important amount of solar radiation received by the central solar receiver cannot be
 433 converted into heat and is thus lost.

434
 435 Table 3-8. Simulation results on energy efficiency of the CSP plant for typical summer and winter days (basic
 436 production mode)
 437

	Reference case	Thermal Int.		Mass Int.		Turbine Int.	
		Summer	Winter	Summer	Winter	Summer	Winter
Global efficiency (%)	21.50	28.15	30.83	27.81	30.80	31.39	31.96
Rankine efficiency (%)	21.51	31.54	31.45	31.55	31.47	34.74	33.05
Rankine efficiency (%) static study [Pelay, 2019]	42.6	30.80		30.00		33.88	

438
 439
 440 Generally speaking, the Rankine efficiency is slightly higher than the global efficiency by
 441 neglecting the losses in the solar circuit. The values of Rankine efficiency obtained by the dynamic
 442 study are close to those obtained in the static study [Pelay, 2019] for all the three Int. concepts (less
 443 than 1% difference). However, the Rankine efficiency of the reference case has halved from 42.6%
 444 to 21.51%. This is because during the static study, the amount of solar energy was considered as
 445 constant all along the day. While in this dynamic study, it is varied all the time. This variability
 446 induces a large amount of lost energy.

447
448

4. Peak production mode

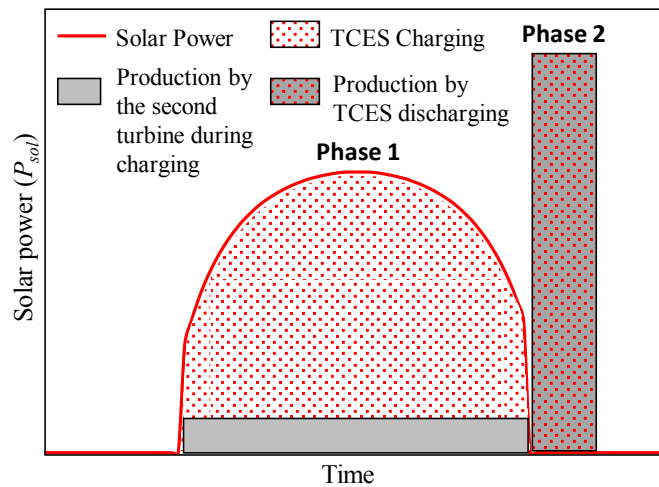
450

451 In this section, the dynamic simulation results for a peak production mode are reported.
452 Contrary to the basic continuous production scenario, the peak production mode aims at a massive
453 electricity production within one or several short periods of time when the electricity selling price is
454 the highest on the spot market [Tapachès, 2019]. It is thus interesting to compare the same TCES
455 Int. concept for two different modes of production. The Turbine Int. concept has been selected for
456 this purpose because it enables the waste heat recovery of overheated vapors via the second turbine
457 when the principal Rankine cycle is not working.

458

459 The operation mode is shown in Fig. 68. During phase 1, the Rankine cycle is at the stop
460 state without electricity production. The TCES reactor is charged and a part of the waste heat of
461 the superheated ~~vapor-steam~~ is valorized as electricity production via the second turbine in the
462 TCES circuit. During phase 2 (peak hour but insufficient sunshine), the stored heat will be all
463 discharged to run the Rankine cycle at about 1000 MW_{el} (10 times of the nominal power), in order
464 to realize a peak power production within about 1 hour.

465



466
467

Figure 68. Schematic view of the operational mode for the peak production mode

468

469

470 Table 49 summarizes all the mains simulation results for a typical summer day under peak
471 and basic production modes. The charging duration of 12.7 hours corresponds to the total sunshine
472 duration (Fig. 48). The discharging duration (1.1 hour) is determined by the size of the TCES reactor
473 which is the same as that for the basic production mode. The second turbine of the TCES circuit
474 produces 550 MW_{h_{el}} during the charging (Phase 1) while the Rankine cycle generates 1002 MW_{h_{el}}
475 during the peak hour.

476

477 Table 49. Dynamic simulation results of Turbine Int. concept for a typical summer day in basic and peak
478 production modes

479

	Basic mode	Peak mode
--	------------	-----------

Efficiency		
Global efficiency (%)	28.15	17.89
Rankine efficiency (%)	31.54	27.96
Storage		
Charge duration (h)	12.3	12.7
Discharge duration (h)	13.06	1.1
Energy produced/ consumed		
Global energy produced (MW.h)	2601	1552
Global energy consumed (MW.h)	304	567
Rankine energy consumed (MW.h)	27	12
Water consumption		
Global water consumption (kton)	333	219

480

481

482

483

484

485

486

487

488

489

490

491

492

493

494

495

496

497

498

5. Conclusion and prospects

499

500

501

502

503

504

505

506

507

508

509

510

511

512

In this study, the dynamic simulation of a CSP plant with TCES system integration have been performed. The Dymola environment has been used with component models existing in the library or developed in-house. Both the basic continuous production mode and the peak production mode have been investigated. Based on the results obtained, main conclusions can be summarized as follows.

- TES integration is needed to increase the output of a CSP plant. Among the three TCES Int. concepts proposed, the Turbine Int. concept has the best global efficiency (31.39% for summer; 31.96% for winter).
- The TCES unit and solar field sized for a typical summer day will be largely oversized when used for a typical winter day.

- 513 • The global electricity consumption of the CSP plant with TCES integration is about 12% of
514 the total electricity production for a typical summer day and about 3% for a typical winter
515 day.
- 516
- 517 • The water consumption of the CSP plant with TCES integration is about 0.12 kton/MW.h_{el}
518 for a typical summer day. For a typical winter day, the water consumption of the Turbine
519 Int. concept is the highest (0.17 kton/MW.h_{el}) compared to the Thermal Int concept (0.14
520 kton/MW.h_{el}) or the Mass Int. concept (0.12 kton/MW.h_{el}).
- 521
- 522 • The peak production mode is achievable by using the Turbine Int. concept. An increased
523 nominal power by a factor of 10 could be reached by discharging the stored heat within one
524 hour. However, a lower global efficiency (17.89%) is rendered due to the higher electricity
525 consumption of the air compressor in the solar circuit. ~~It will then be interesting to carry
526 out a techno-economic study for different integrations and modes of production~~
- 527

528 One limitation of the current study is that the simulations are based on two perfect summer
529 and winter days while the effect of cloud passages has not been considered yet. Nevertheless, the
530 simulations showed that the large thermal inertia of the TCES unit, owing to the great quantity of
531 stainless steel ($\sim 1.2 \times 10^7$ kg) and reactive salts ($\sim 1.1 \times 10^7$ kg) involved, can allow a quick
532 charging/discharging switch and maintain a constant output of the Rankine power cycle. A future
533 work using real DNI curves surveyed for some typical cloudy days will provide more details on
534 influence of the short DNI variation.

535

536 Another simplification made is that the DNI value has not been corrected with the cosine
537 loss, which could have a non-negligible impact on the simulation results: about 5% in summer and
538 30% in winter based on the estimation of Peng et al., [2013]. Taking into account the cosine loss
539 would increase the size of solar field (designed for a perfect summer day) and thereby decrease the
540 electricity production of the winter day. This matter of concern should be addressed in the future
541 studies.

542

543 It should be noted that this study has focused on the energy modeling and dynamic
544 simulation of the CSP plant, under the basic and peak operation modes. The improvement of the
545 models used for the simulations and their parameter remains an important objective. A real power
546 parasitic consumption of the turbomachines (turbines, pumps and compressor) would be obtained
547 with variables isentropic efficiencies. Futures experiments will also enable the use of a real
548 stoichiometric reaction coefficient for the thermochemical reactor. Furthermore, a techno-economic
549 assessment is also suggested in the future study to further understand the usability and the cost-
550 effectiveness of the proposed TCES integration concepts. Recent advances on the techno-economic
551 issue can be found in Refs [Salas, 2018; Tapachès; 2019].

552

553

554

555 **Acknowledgement**

556
557
558
559
560
561
562
563
564
565
566
567
568
569
570
571
572
573
574
575
576
577
578
579
580
581
582
583
584
585
586
587
588
589
590
591
592
593

This work is supported by the French ANR within the project In-STORES (ANR-12-SEED-0008).

Appendix A. Detailed description of the in-house developed models

~~Appendix B. Parameter values and variables fixed by the user for the dynamic simulation~~

Nomenclature

Latin letters

H	charging or discharging time, h
P	power, W
Q	heat exchange rate, W
W	work exchange rate, W
T	temperature, K
t	time, s
X	reaction progress, (-)

Greek symbols

η	energy efficiency
Δh_R	specific reaction heat, kJ.kg ⁻¹

Subscripts

C	charging stage
CP	compressor
D	discharging stage
el	electricity
$Global$	Whole system
P	pump
R	reactor
$Rankine$	Rankine circuit
SG	steam generator
sol	solar
T	turbine

594 **References**

- 595
596 Albanakis, C., Missirlis, D., Michailidis, N., Yakinthos, K., Goulas, A., Omar, H., Tsipas, D., Granier, B. (2009).
597 Experimental analysis of the pressure drop and heat transfer through metal foams used as volumetric receivers
598 under concentrated solar radiation. *Experimental Thermal and Fluid Science*, 33(2), 246–252.
599 <https://doi.org/10.1016/j.expthermflusci.2008.08.007>
600
- 601 Alovio, A., Chacartegui, R., Ortiz, C., Valverde, J.M., Verda, V. (2017). Optimizing the CSP Calcium Looping
602 integration for Thermochemical Energy Storage. *Energy Conversion and Management*, 136, 85–98.
603 doi:10.1016/j.enconman.2016.12.093.
604
- 605 Altés Buch, Q. (2014). *Dynamic modeling of a steam Rankine Cycle for Concentrated Solar Power applications*.
606 Master thesis, University of Liege.
607
- 608 Alva, G., Lin, Y., & Fang, G. (2018). An overview of thermal energy storage systems. *Energy*. 144, 341-378.
609 <https://doi.org/10.1016/j.energy.2017.12.037>
610
- 611 Batuecas, E., Mayo, C., Díaz, R., & Pérez, F. J. (2017). Life Cycle Assessment of heat transfer fluids in parabolic
612 trough concentrating solar power technology. *Solar Energy Materials and Solar Cells*, 171, 91–97.
613 <https://doi.org/10.1016/j.solmat.2017.06.032>
614
- 615 Cabeza, L. F., Solé, A., Fontanet, X., Barreneche, C., Jové, A., Gallas, M., Fernández, A. I. (2017).
616 Thermochemical energy storage by consecutive reactions for higher efficient concentrated solar power plants
617 (CSP): Proof of concept. *Applied Energy*, 185, 836–845. <https://doi.org/10.1016/j.apenergy.2016.10.093>
618
- 619 Das D., Sinha N., Roy K., Automatic generation control of an organic Rankine cycle solar-thermal/wind-
620 diesel hybrid energy system. *Energy technology*, 2, 721-731.
621 <https://onlinelibrary.wiley.com/doi/abs/10.1002/ente.201402024>
622
- 623 Dassault Systèmes AB. (2011). *User Manual*. Dymola (Dynamic Modeling Laboratory)
624
- 625 Ding, W., Shi, H., Jianu, A., Xiu, Y., Bonk, A., Weisenburger, A., & Bauer, T. (2019). Molten chloride salts
626 for next generation concentrated solar power plants: Mitigation strategies against corrosion of structural
627 materials. *Solar Energy Materials and Solar Cells*, 193, 298–313. <https://doi.org/10.1016/j.solmat.2018.12.020>
628
- 629 Gimenez, P., & Fereres, S. (2015). Effect of Heating Rates and Composition on the Thermal Decomposition
630 of Nitrate Based Molten Salts. *Energy Procedia*, 69, 654–662. <https://doi.org/10.1016/j.egypro.2015.03.075>
631
- 632 IEA (2018). *World Energy Outlook (WEO) 2018*, International Energy Agency. ISBN: 978-92-64-30677-6.
633
- 634 IRENA (2018). *Renewable Power Generation Costs in 2017*. International Renewable Energy Agency.
635 https://www.irena.org/-/media/Files/IRENA/Agency/Publication/2018/Jan/IRENA_2017_Power_Costs_2018.pdf
636
- 637 Jarimi, H., Aydin, D., Yanan, Z., Ozankaya, G., Chen, X., & Riffat, S. (2019). Review on the recent progress
638 of thermochemical materials and processes for solar thermal energy storage and industrial waste heat recovery.
639 *International Journal of Low-Carbon Technologies*, 14, 44-69. <https://doi.org/10.1093/ijlct/cty052>
640
- 641 Khalanski, M., Gras, R. (1996). Rejets en rivières et hydrobiologie – Un aperçu sur l'expérience française. *La*
642 *houille blanche*. <http://dx.doi.org/10.1051/lhb/1996046>
643
- 644 Kuravi, S., Trahan, J., Goswami, D. Y., Rahman, M. M., & Stefanakos, E. K. (2013, August). Thermal energy
645 storage technologies and systems for concentrating solar power plants. *Progress in Energy and Combustion Science*.
646 <https://doi.org/10.1016/j.pecs.2013.02.001>
647
- 648 Larrouturou, F., Caliot, C., & Flamant, G. (2014). Effect of directional dependency of wall reflectivity and
649 incident concentrated solar flux on the efficiency of a cavity solar receiver. *Solar Energy*, 109(1), 153–164.
650 <https://doi.org/10.1016/j.solener.2014.08.028>
651

652 Lin, Y., Alva, G., & Fang, G. (2018). Review on thermal performances and applications of thermal energy
653 storage systems with inorganic phase change materials. *Energy*, 165, 685-708.
654 <https://doi.org/10.1016/j.energy.2018.09.128>
655

656 Liu, D., Xin-Feng, L., Bo, L., Si-quan, Z., & Yan, X. (2018). Progress in thermochemical energy storage for
657 concentrated solar power: A review. *International Journal of Energy Research*, 42, 4546-4561.
658 <https://doi.org/10.1002/er.4183>
659

660 Lu, W., Zhao, C. Y., & Tassou, S. A. (2006). Thermal analysis on metal-foam filled heat exchangers. Part I:
661 Metal-foam filled pipes. *International Journal of Heat and Mass Transfer*, 49(15-16), 2751-2761.
662 <https://doi.org/10.1016/j.ijheatmasstransfer.2005.12.012>
663

664 Martiensen, W., Warlimont, H. (2005). Springer handbook of condensed matter and materials data. *Springer*
665 *handbooks*. eReference ISBN 978-3-540-30437-1.
666

667 Mazet, N., & Amouroux, M. (1991). Analysis of heat transfer in a non-isothermal solid-gas reacting medium.
668 *Chemical Engineering Communications*, 99(1), 175-200. <https://doi.org/10.1080/00986449108911586>
669

670 MBL (2018). Modelica Buildings library - Open source library for building energy and control systems.
671 <http://simulationresearch.lbl.gov/modelica/index.html>
672

673 Mohan, G., Venkataraman, M. B., & Coventry, J. (2019). Sensible energy storage options for concentrating
674 solar power plants operating above 600 °C. *Renewable and Sustainable Energy Reviews*, 107, 319-337.
675 <https://doi.org/10.1016/j.rser.2019.01.062>
676

677 MTES (1998). Ministère de la transition écologique et solidaire (1998). Circulaire du 06/06/53 relative au
678 rejet des eaux résiduaires par les établissements classés comme dangereux, insalubres ou incommodes en
679 application de la loi du 19 décembre 1917 (abrogée). AIDA. https://aida.ineris.fr/consultation_document/8589
680

681 Nazir, H., Batool, M., Bolivar Osorio, F. J., Isaza-Ruiz, M., Xu, X., Vignarooban, K., Phelan, P., Inamuddin,
682 Kannan, A. M. (2019). Recent developments in phase change materials for energy storage applications: A review.
683 *International Journal of Heat and Mass Transfer*, 129, 491-523.
684 <https://doi.org/10.1016/j.ijheatmasstransfer.2018.09.126>
685

686 NREL (2018). *Concentrating Solar Power Projects 2017*. National Renewable Energy Laboratory
687 <https://www.nrel.gov/csp/solarpaces/index.cfm>
688

689 Nunes, V. M. B., Lourenço, M. J. V., Santos, F. J. V., & Nieto de Castro, C. A. (2019). Molten alkali carbonates
690 as alternative engineering fluids for high temperature applications. *Applied Energy*, 242, 1626-1633.
691 <https://doi.org/10.1016/j.apenergy.2019.03.190>
692

693 Ortiz, C., Chacartegui, R., Valverde, J. M., Alovio, A., & Becerra, J. A. (2017). Power cycles integration in
694 concentrated solar power plants with energy storage based on calcium looping. *Energy Conversion and*
695 *Management*, 149, 815-829. <https://doi.org/10.1016/j.enconman.2017.03.029>
696

697 Ortiz, C., Romano, M. C., Valverde, J. M., Binotti, M., Chacartegui, R. (2018). Process integration of Calcium-
698 Looping thermochemical energy storage system in concentrating solar power plants. *Energy*, 155, 535-551.
699 doi:10.1016/j.energy.2018.04.180
700

701 Ortiz, C., Valverde, J. M., Chacartegui, R., Perez-Maqueda, L. A., & Giménez, P. (2019). The Calcium-Looping
702 (CaCO₃/CaO) process for thermochemical energy storage in Concentrating Solar Power plants. *Renewable and*
703 *Sustainable Energy Reviews*, 113, 1364-0321. <https://doi.org/10.1016/j.rser.2019.109252>
704

705 Pelay, U., Luo, L., Fan, Y., Stitou, D., & Castelain, C. (2019). Integration of a thermochemical energy storage
706 system in a Rankine cycle driven by concentrating solar power: Energy and exergy analyses. *Energy*, 167, 498-
707 510. <https://doi.org/10.1016/j.energy.2018.10.163>
708

709 Pelay, U., Luo, L., Fan, Y., Stitou, D., & Rood, M. (2017a). Thermal energy storage systems for concentrated
710 solar power plants. *Renewable and Sustainable Energy Reviews*, 79, 82-100.
711 <https://doi.org/10.1016/j.rser.2017.03.139>

712 Pelay, U., Luo, L., Fan, Y., Stitou, D., & Rood, M. (2017b). Technical data for concentrated solar power plants
713 in operation, under construction and in project. *Data in Brief*, 13, 597–599.
714 <https://doi.org/10.1016/j.dib.2017.06.030>
715

716 Peng, S., Hong, H., Jin, H., & Zhang, Z. (2013). A new rotatable-axis tracking solar parabolic-trough collector
717 for solar-hybrid coal-fired power plants. *Solar Energy*, 98(PC), 492–502.
718 <https://doi.org/10.1016/j.solener.2013.09.039>
719

720 Prieto, C., Cooper, P., Fernandez, A.I., & Cabeza, L. F. (2016). Review of technology: thermochemical energy
721 storage for concentrated solar power plants. *Renewable and Sustainable Energy Reviews*, 60, 909-929.
722 <https://doi.org/10.1016/j.rser.2015.12.364>.
723

724 PVGIS. Photovoltaic Geographical Information System (PVGIS). <http://re.jrc.ec.europa.eu/pvgis.html>
725

726 Quoilin, S., Desideri, A., Wronski, J., & Bell, I. (2017). *ThermoCycle Library*. <http://www.thermocycle.net/>
727

728 Qureshi, Z. A., Ali, H. M., & Khushnood, S. (2018). Recent advances on thermal conductivity enhancement
729 of phase change materials for energy storage system: A review. *International Journal of Heat and Mass Transfer*,
730 127, 838-856. <https://doi.org/10.1016/j.ijheatmasstransfer.2018.08.049>
731

732 Salas, D., Tapachès, E., Mazet, N., & Aussel, D. (2018). Economical optimization of thermochemical storage
733 in concentrated solar power plants via pre-scenarios. *Energy Conversion and Management*, 174, 932–954.
734 <https://doi.org/10.1016/j.enconman.2018.08.079>
735

736 Schmidt, M., & Linder, M. (2017). Power generation based on the Ca(OH)₂/ CaO thermochemical storage
737 system – Experimental investigation of discharge operation modes in lab scale and corresponding conceptual
738 process design. *Applied Energy*, 203, 594–607. <https://doi.org/10.1016/j.apenergy.2017.06.063>
739

740 Tao, Y. B., & He, Y. L. (2018). A review of phase change material and performance enhancement method
741 for latent heat storage system. *Renewable and Sustainable Energy Reviews*, 93, 245-259.
742 <https://doi.org/10.1016/j.rser.2018.05.028>
743

744 Tapachès, E., Salas, D., Perier-Muzet, M., Mauran, S., Aussel, D., & Mazet, N. (2019). The value of
745 thermochemical storage for concentrated solar power plants: Economic and technical conditions of power plants
746 profitability on spot markets. *Energy Conversion and Management*. <https://doi.org/10.1016/j.enconman.2018.11.082>
747

748 Vidil, R., Grillot, J. M., Marvillet, C., Mercier, P., & Ratel, G. (1990). *Les échangeurs à plaques : description et*
749 *éléments de dimensionnement*. 2nd edition, Lavoisier Tec & Doc Distribution, Paris, France.
750

751 Vignarooban, K., Xu, X., Arvay, A., Hsu, K., & Kannan, A. M. (2015). Heat transfer fluids for concentrating
752 solar power systems - A review. *Applied Energy*, 146, 383–396. <https://doi.org/10.1016/j.apenergy.2015.01.125>
753

754 Villada, C., Bonk, A., Bauer, T., & Bolívar, F. (2018). High-temperature stability of nitrate/nitrite molten salt
755 mixtures under different atmospheres. *Applied Energy*, 226, 107–115.
756 <https://doi.org/10.1016/j.apenergy.2018.05.101>
757

758 Villada, C., Jaramillo, F., Castaño, J. G., Echeverría, F., & Bolívar, F. (2019). Design and development of nitrate-
759 nitrite based molten salts for concentrating solar power applications. *Solar Energy*, 188, 291–299.
760 <https://doi.org/10.1016/j.solener.2019.06.010>
761

762 Walczak, M., Pineda, F., Fernández, Á. G., Mata-Torres, C., & Escobar, R. A. (2018). Materials corrosion for
763 thermal energy storage systems in concentrated solar power plants. *Renewable and Sustainable Energy Reviews*, 86,
764 22-44. <https://doi.org/10.1016/j.rser.2018.01.010>
765

766 Wang, W., Guan, B., Li, X., Lu, J., & Ding, J. (2019). Corrosion behavior and mechanism of austenitic stainless
767 steels in a new quaternary molten salt for concentrating solar power. *Solar Energy Materials and Solar Cells*, 194,
768 36–46. <https://doi.org/10.1016/j.solmat.2019.01.024>
769

770

771 Wu, Z., Caliot, C., Bai, F., Flamant, G., Wang, Z., Zhang, J., & Tian, C. (2010). Experimental and numerical
772 studies of the pressure drop in ceramic foams for volumetric solar receiver applications. *Applied Energy*, 87(2),
773 504–513. <https://doi.org/10.1016/j.apenergy.2009.08.009>

774
775 Zhao, C. Y., Kim, T., Lu, T. J., & Hodson, H. P. (2001). *Thermal Transport Phenomena in Porvair Metal Foams*
776 *and Sintered Beds*, Ph.D. report, University of Cambridge.

777

778 **List of Figures.**

- 779
- 780 [Figure 1. Schematic view of the reference SPT plant without TES. Adapted from \[Pelay, 2019\]](#)
- 781
- 782 [Figure 2. Schematic view of the SPT plant with TCES integration. \(a\) Thermal Int. concept; \(b\) Mass Int. concept;](#)
- 783 [\(c\) Turbine Int. concept. Adapted from \[Pelay, 2019\]](#)
- 784
- 785 [Figure 3. Average DNI for a typical summer and a winter day at eastern Pyrenees \(42.497N, 1.959E\) \[PVGIS\]](#)
- 786
- 787 [Figure 4. Schematic view of the operational mode divided into 3 phases for the basic continuous production](#)
- 788 [mode](#)
- 789
- 790 [Figure 5. Charging/discharging durations for different integration concepts](#)
- 791
- 792 [Figure 6. Ratio of electricity consumption to production for the CSP plant with different TCES integration](#)
- 793 [concepts \(\$MW_{el\ consumed}/MW_{el\ produced}\$ \)](#)
- 794
- 795 [Figure 7. Water consumption \(\$kton/MW_{el}\$ \) of the CSP plant with different TCES integration concepts](#)
- 796
- 797 [Figure 8. Schematic view of the operational mode for the peak production mode](#)
- 798
- 799 [Figure A1. Schematic view of the plat-type TCES reactor. \(a\) charging; \(b\) discharging](#)
- 800
- 801 [Figure A2. Schematic diagram of the TCES reactor created in the Dymola environment](#)
- 802
- 803 [Figure A3. Schematic diagram of the volumetric solar receiver created in the Dymola environment](#)
- 804
- 805

806 **List of Tables.**

- 807
- 808 [Table 1. Component model of the CSP plant with TCES integration used for the dynamic modeling](#)
- 809
- 810 [Table 2. List of all PID controllers](#)
- 811
- 812 [Table 3. Sizing of the solar field for different TCES integration concepts](#)
- 813
- 814 [Table 4. Parameter values for different components of the system](#)
- 815
- 816 [Table 5. Variables fixed by user - Phase 1](#)
- 817
- 818 [Table 6. Variables fixed by user - Phase 2](#)
- 819
- 820 [Table 7. Variables fixed by user - Phase 3](#)
- 821
- 822 [Table 8. Simulation results on energy efficiency of the CSP plant for typical summer and winter days \(basic](#)
- 823 [production mode\)](#)
- 824
- 825 [Table 9. Dynamic simulations results of Turbine Int. concept for a typical summer day in basic and peak](#)
- 826 [production modes](#)
- 827
- 828 [Table B1. List of all PID controllers](#)
- 829
- 830 [Table B2. Parameter values for different components of the system](#)
- 831
- 832 [Table B3. Variables fixed by user - Phase 1](#)
- 833
- 834 [Table B4. Variables fixed by user - Phase 2](#)
- 835
- 836 [Table B5. Variables fixed by user - Phase 3](#)

837

838 **Appendix A. Detailed description of the in-house developed models**

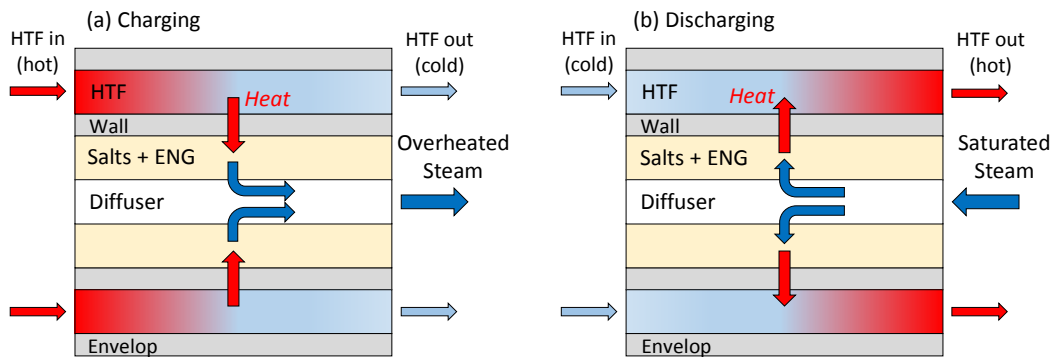
839

840 *A1. Modeling of the TCES reactor*

841

842 The TCES reactor is the most crucial element of the whole system, having the largest
 843 thermal inertia. It is designed based on the concept of a plate heat exchanger-reactor as shown in
 844 Fig. A1. There are four main parts that constitute the TCES reactor: (i) the mixture of salts
 845 ($\text{Ca}(\text{OH})_2/\text{CaO}$) and the expanded natural graphite (ENG) as the reactive/storage material; (ii) the
 846 HTF channels; (3) the metal wall separating the reactive salts and the HTF; and (iv) the dead
 847 volume comprising the composite porosities, the diffuser and the envelop. Figure A2 shows the
 848 schematic of the TCES reactor created in the Dymola environment. The modeling of heat and mass
 849 transfers in this TCES reactor is presented as follows.

850

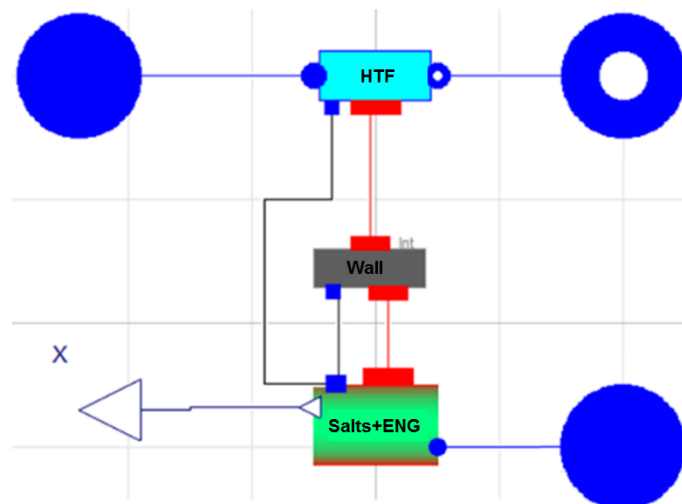


851
852

Figure A1. Schematic view of the plat-type TCES reactor. (a) charging; (b) discharging

853

854



855
856

Figure A2. Schematic diagram of the TCES reactor created in the Dymola environment

857

858

- The reactive bloc

859

860 The reactive bloc is composed of the composite (salts and ENG) and the dead volume. Heat
 861 transfer occurs between the composite, the dead volume and the wall whereas mass transfer occurs
 862 between the composite and the dead volume. A nodal model was used for the modeling of the
 863 reactive bloc. The heat conduction between the reactive salts and the dead volume is neglected by
 864 assuming the identical temperature. The heat absorbed or released by the reactive salts is transferred
 865 to the wall by heat conduction and convection. During the synthesis, a certain amount of heat
 866 (named as Q_{sens}) released by the reaction is used to raise the steam temperature entering in the
 867 TCES reactor up to the equilibrium temperature. The thermal balance of reactive bloc may be
 868 written as Eqs. (A1) and (A2).

$$m_{comp} \cdot Cp_{comp} \cdot \frac{dT_{comp}}{dt} = H_{W/comp} \cdot S_{W/comp} \cdot (T_W - T_{comp}) - \Delta h_{R_{comp}} \cdot \frac{dn_{H_2O}}{dt} + Q_{sens} \quad (A1)$$

$$Q_{sens} = \dot{m}_{H_2O} \cdot (h_{R_{ext}} - h_{R_{int}}) \quad (A2)$$

869 with m_{comp} , the composite mass (kg)
 870 Cp_{comp} , the specific heat of the composite ($J \cdot kg^{-1} \cdot K^{-1}$)
 871 T_{comp} , the temperature of the composite (K)
 872 T_W , the wall temperature (K)
 873 $H_{W/comp}$, the heat transfer coefficient between the wall and the composite ($W \cdot m^{-2} \cdot K^{-1}$)
 874 $S_{W/comp}$, the contact surface area between the wall and the composite (m^2)
 875 $\Delta h_{R_{comp}}$, the molar reaction heat of the $Ca(OH)_2/CaO$ couple ($104 \text{ kJ} \cdot \text{mol}^{-1}$)
 876 n_{H_2O} , the mole number of H_2O reacted with the CaO salt (mol)
 877 \dot{m}_{H_2O} , the vapor mass flow-rate ($kg \cdot s^{-1}$)
 878 $h_{R_{int}}$, $h_{R_{ext}}$ the enthalpy of the vapor at the interior and outside of the TCES reactor,
 879 respectively ($J \cdot kg^{-1}$)

880
 881 The vapor mass flow-rate (\dot{m}_{H_2O}) entering/exiting the TCES reactor is directly dependent
 882 on the reaction rate, calculated by Eqs. (A3) and (A4).

$$\dot{m}_{H_2O} = M_{H_2O} \cdot \frac{dn_{H_2O}}{dt} \quad (A3)$$

$$\frac{dn_{H_2O}}{dt} = -\gamma_R \cdot n_{salt} \cdot \frac{dX}{dt} \quad (A4)$$

883 with M_{H_2O} , the H_2O molar mass ($kg \cdot mol^{-1}$)
 884 γ_R , the global reactor efficiency (-)
 885 n_{salt} , the salt molar quantity (mol)
 886 X , the molar reaction progress

887
 888 The reaction progress is calculated by the kinetic model proposed by Mazet and Amouroux
 889 [Mazet, 1991] for the decomposition (Eq. A5) and for the synthesis (Eq. A6), respectively.

$$\frac{dX}{dt} = K_{cin} \cdot X \cdot \frac{p_{op} - p_{eq}}{P_{op}} \quad (A5)$$

$$\frac{dX}{dt} = K_{cin} \cdot (1 - X) \cdot \frac{p_{op} - p_{eq}}{p_{op}} \quad (\text{A6})$$

890 with K_{cin} , the reaction kinetic coefficient (s^{-1})
 891 p_{op} , the operational pressure (Pa)
 892 p_{eq} , the equilibrium pressure (Pa)

893
 894 The reaction kinetic coefficient (K_{cin}) is chosen be to equal to $5 \times 10^{-3} \text{ s}^{-1}$ at a first time,
 895 subjected to possible modifications during the simulations [Mazet, 1991]. The equilibrium pressure
 896 p_{eq} is determined with the Clapeyron equation represented by Eq. (A7) and simplified as Eq. (A8).

$$\ln\left(\frac{p_{eq}}{p_{ref}}\right) = \frac{\Delta h_{Rcomp}}{R} \left(\frac{1}{T_{ref}} - \frac{1}{T_{eq}}\right) \quad (\text{A7})$$

$$p_{eq} = p_{ref} \cdot e^{\frac{\Delta H_{Rcomp}}{R} \left(\frac{1}{T_{ref}} - \frac{1}{T_{eq}}\right)} \quad (\text{A8})$$

897 With p_{ref} , the reference pressure (1 bar)
 898 R , the ideal gas constant ($8.314 \text{ J} \cdot \text{mol}^{-1} \cdot \text{K}^{-1}$)
 899 T_{ref} , the reference temperature (298.15 K)
 900 T_{eq} , the equilibrium temperature (773.15 K)

901
 902 The term $\frac{p_{op} - p_{eq}}{p_{op}}$ represents the difference between the operational and the equilibrium
 903 conditions as the driving force for the reaction.

904
 905 The physical properties of the composite depend on the temperature, the percentage of ENG
 906 and the reaction rate. Three parameters were used to settle simple equations to calculate various
 907 physical properties of the composite:

- 908 - $m_{salt(0)}$ the anhydrous salt mass (CaO) at the initial state (kg);
- 909 - $\tilde{\rho}_{ENG}$ the ENG apparent density ($\text{kg} \cdot \text{m}^{-3}$);
- 910 - τ_{salt} the mass ratio of reactive salt in the composite, defined as Eq. (A9).

$$\tau_{salt} = \frac{m_{salt(0)}}{m_{comp(0)}} \quad (\text{A9})$$

911 m_{comp} is the mass of the composite composed of reactive salts and the ENG:

$$m_{comp} = m_{salt} + m_{ENG} \quad (\text{A10})$$

$$m_{ENG} = (1 - \tau_{salt}) \times m_{comp(0)} \quad (\text{A11})$$

912
 913 The mass of reactive salts in the TCES reactor depends on the reaction progress, shown in
 914 Eq. (A12):

$$m_{salt} = n_{salt(0)} \cdot (X \cdot M_{Ca(OH)_2} + (1 - X) \cdot M_{CaO}) \quad (\text{A12})$$

915 with m_{salt} , the salt mass (kg)

916 n_{salt} , the salt molar quantity (mol)
 917 X , the molar progress
 918 $M_{Ca(OH)_2}$, the $Ca(OH)_2$ molar mass ($kg \cdot mol^{-1}$)
 919 M_{CaO} , the CaO molar mass ($kg \cdot mol^{-1}$)
 920

921 The specific heat of the composite varies according to its temperature and its composition,
 922 calculated by Eq. (A13):

$$Cp_{comp} = \tau_{salt} \cdot \left((1 - X) \cdot Cp_{CaO} + X \cdot Cp_{Ca(OH)_2} \right) + (1 - \tau_{salt}) \cdot Cp_{ENG} \quad (A13)$$

923 where Cp_{CaO} and $Cp_{Ca(OH)_2}$ are determined by Eq. (A14) and Eq. (A15), respectively
 924 [Martienssen, 2005].
 925

$$Cp_{CaO} = 0.16495 \times T + 798.647 \quad (A14)$$

$$Cp_{Ca(OH)_2} = 0.38612 \times T + 1217.29416 \quad (A15)$$

926
 927 The volume of the composite used for the sizing of the TCES reactor is determined by Eq.
 928 (A16):

$$V_{comp} = \frac{(1 - \tau_{salt}) \cdot m_{salt(0)}}{\tau_{sel} \cdot \tilde{\rho}_{ENG}} \quad (A16)$$

929
 930 The porosity ε is the ratio of dead volume and composite volume, calculated by Eq. (A17):

$$\varepsilon = 1 - \frac{\tilde{\rho}_{ENG}}{\rho_{ENG}} - \tilde{\rho}_{ENG} \cdot \frac{\tau_{salt}}{1 - \tau_{salt}} \cdot \frac{X \cdot Vm_{salt(X=1)} + (1 - X) \cdot Vm_{salt(X=0)}}{M_{salt(0)}} \quad (A17)$$

931 with: $Vm_{sel(X=1)} = Vm_{Ca(OH)_2}$

932 $Vm_{sel(X=1)} = Vm_{CaO}$

933 $M_{sel(0)} = M_{CaO}$

934 ρ_{ENG} , the GNE density ($kg \cdot m^{-3}$)

935 $\tilde{\rho}_{ENG}$, the GNE apparent density ($kg \cdot m^{-3}$)

936 V_m , the molar volume ($m^3 \cdot mol^{-1}$)
 937

938 • The dead volume (DV)
 939

940 The dead volume corresponds to all the unoccupied volume in the TCES reactor, including
 941 void volume of the composite material and the gas diffuser, calculated by Eq. (A18):

$$V_{DV} = \varepsilon \cdot V_{comp} + V_{diffuser} \quad (A18)$$

942
943
944
945

The volume of diffuser depends on the reactor geometry. For a plate-type heat exchanger, it is calculated according to the total surface area of the plates (S_W) and the fixed diffuser thickness ($th_{diffuser}$), by Eq. (A19):

$$V_{diffuser} = \frac{S_W}{2} \cdot th_{diffuser} \quad (A19)$$

946
947
948

The vapor flowrate variation $d\dot{m}$ is the difference between the entering flowrate (\dot{m}_{in}) and the outgoing flowrate (\dot{m}_{out}). Mass conservation equation in the DV can be written as.

$$d\dot{m} = \dot{m}_{in} - \dot{m}_{out} \quad (A20)$$

$$d\dot{m} = V_{DV} \cdot \left(\frac{dh}{dt} \cdot \frac{d\rho}{dh} \Big|_p + \frac{dP}{dt} \cdot \frac{d\rho}{dP} \Big|_h \right) \quad (A21)$$

949
950
951
952
953

With \dot{m} , the mass flow-rate ($\text{kg}\cdot\text{s}^{-1}$)
 h , the mass enthalpy ($\text{kJ}\cdot\text{kg}^{-1}$)
 ρ , the density ($\text{kg}\cdot\text{m}^{-3}$)

The energy conservation in the DV is calculated with Eq. (A22):

$$\left(\frac{V_{DV} \cdot p_{op} \cdot M_{H_2O}}{R \cdot T_{comp}} \right) \cdot \left(\left(\frac{1}{p_{op}} \cdot \frac{dp}{dt} + \frac{1}{T_{comp}} \right) \cdot \left(C_{p_{H_2O}} \cdot (T_{comp} - T_{ref}) - \frac{R \cdot T_{comp}}{M_{H_2O}} \right) + \frac{dT_{comp}}{dt} \cdot \left(C_{p_{H_2O}} - \frac{R}{M_{H_2O}} \right) \right) = \frac{d\dot{m}}{dt} \cdot h_{comp} \quad (A22)$$

954
955
956
957
958
959
960
961
962
963
964
965

with, V_{DV} , the dead volume volume (m^3)
 T_{comp} , the composite temperature (K)
 p , the pressure (Pa)
 T_{comp} , the composite temperature (K)
 $C_{p_{H_2O}}$, the H_2O mass specific heat capacity ($\text{J}\cdot\text{kg}^{-1}\cdot\text{K}^{-1}$)

- The wall

A nodal model was used for the wall, assuming uniform temperature and constant specific heat. The thermal inertia of the model was however taken into account. The total exchange area can be calculated with Eq. (A23):

$$S_W = \frac{V_{comp}}{th_{comp}} \quad (A23)$$

966

The total wall mass (m_w) can then be determined with Eq. (A24).

$$m_w = th_w \cdot S_W \cdot \rho_w \quad (A24)$$

967 where th_w is the thickness of the wall fixed by the designer. ρ_w is the density of the wall
 968 material.

969

970 The energy conservation is represented Eq. (A25)

$$m_w \cdot Cp_w \cdot \frac{dT_w}{dt} = S_{ext} \cdot \varphi_{out} + S_{int} \cdot \varphi_{in} \quad (A25)$$

971 with φ_e , the entering flux ($W \cdot m^{-2}$)

972 φ_e , the outgoing flux ($W \cdot m^{-2}$)

973 m_w , the wall mass (kg)

974 Cp_w , the wall mass specific heat capacity ($J \cdot kg^{-1} \cdot K^{-1}$)

975 T_w , the wall temperature (K)

976 S_{ext} , the exterior surface (m^2)

977 S_{int} , the interior surface (m^2)

978

979

980 • HTF

981

982 The HTF part permits the entering of HTF (pressurized air) from one side and leaving from
 983 the other side to exchange the heat with the wall part during charging and discharge periods. Since
 984 no phase change is occurred during the cooling/heating of the HTF, a “light non-discretized model”
 985 was chosen for modeling the HTF part. The outlet temperature (T_{out}) of the HTF is determined by
 986 Eq. A26, using the NUT (Number of Unity of Transfer) method.

$$T_{out} = T_{in} - (T_{in} - T_{out}) \cdot \left(1 - e^{\left(\frac{H_{HTF} \cdot S_{R/HTF}}{\dot{m}_{HTF} \cdot Cp_{HTF}} \right)} \right) \quad (A26)$$

987 with T_{out} , the outlet temperature (K)

988 T_{in} , the inlet temperature (K)

989 H_{HTF} , the HTF heat transfer coefficient ($W \cdot m^{-2} \cdot K^{-1}$)

990 $S_{R/HTF}$, the exchange surface area between the HTF and the reactor (m^2)

991 \dot{m}_{HTF} , the HTF mass flow-rate ($kg \cdot s^{-1}$)

992 Cp_{HTF} , the HTF mass specific heat capacity ($J \cdot kg^{-1} \cdot K^{-1}$)

993

994 H_{HTF} , the convective heat transfer coefficient is calculated by using the plate heat exchanger
 995 correlations [Vidil, 1990], shown in Eqs. (A27-A28):

$$Nu = 0.212 \cdot Re^{0.638} \cdot Pr^{0.33} \quad (A27)$$

$$H = \frac{Nu \cdot \lambda}{L_c} \quad (A28)$$

996 with Re , the Reynolds number

997 Pr , the Prandlt number

998 Nu , the Nusselt number

999 H , the heat transfer coefficient ($W \cdot m^{-2} \cdot K^{-1}$)

1000 L_c , the characteristic length (m)

1001 λ , the thermal conductivity ($\text{W}\cdot\text{m}^{-1}\cdot\text{K}^{-1}$)

1002

1003 The Reynold number Re and Prandt number Pr were calculated by Eq. (A29) and Eq. (A30),
1004 respectively.

$$Re = \frac{u_{HTF} \cdot L_c}{\nu} \quad (\text{A29})$$

$$Pr = \frac{Cp_{HTF} \cdot \mu_{HTF}}{\lambda_{HTF}} \quad (\text{A30})$$

1005 with u_{HTF} , the HTF velocity ($\text{m}\cdot\text{s}^{-1}$)

1006 ν_{HTF} the HTF kinematic viscosity ($\text{m}^2\cdot\text{s}^{-1}$)

1007 λ_{HTF} the HTF thermal conductivity ($\text{W}\cdot\text{m}^{-1}\cdot\text{K}^{-1}$)

1008 μ_{HTF} the HTF dynamic viscosity ($\text{J}\cdot\text{s}\cdot\text{m}^{-2}$)

1009 Cp_{HTF} the HTF specific heat ($\text{J}\cdot\text{kg}^{-1}\cdot\text{K}^{-1}$)

1010 L_c the characteristic length of the HTF side plates (m)

1011

1012 Pressure loss (Δp) induced by the HTF are calculated with heat plate exchanger correlations

$$\Delta p = f \cdot \frac{L_p}{D_h} \cdot \rho \cdot \frac{u^2}{2} \quad (\text{A31})$$

1013 with f , the friction factor

1014 L_p , the pipe length (m)

1015 D_h , the hydraulic diameter (m)

1016 ρ , the density ($\text{kg}\cdot\text{m}^{-3}$)

1017 u , the fluid mean velocity ($\text{m}\cdot\text{s}^{-1}$)

1018

1019 The friction factor f is a function of the Re , shown in Eq. (32) [Vidil, 1990]:

$$f = \begin{cases} -3.0812 \cdot 10^{-6} \cdot Re^3 + 7.4857 \cdot 10^{-4} \cdot Re^2 - 6.798 \cdot 10^{-2} \cdot Re + 2.89; & \text{if } Re < 40 \\ 23.33 \cdot Re^{-0.809}; & \text{if } 40 \leq Re < 500 \\ 0.557 \cdot Re^{-0.211}; & \text{if } Re \geq 500 \end{cases} \quad (\text{A32})$$

1020

1021

1022 *A2. Modeling of the solar receiver*

1023

1024 The central solar receiver of the CSP plant absorbs and converts the sunlight into heat, and
1025 transfers it to the HTF flowing through it. It was modeled as a volumetric receiver made of metallic
1026 foam. Figure A3 shows the schematic view of the solar receiver model created in the Dymola
1027 environment, composed of one receiver element absorbing the solar flux, one heater element
1028 transmitting the solar heat to the HTF and another element representing the pressures drops. To
1029 simplify the modeling, the following assumptions were made:

1030 - No thermal inertia;

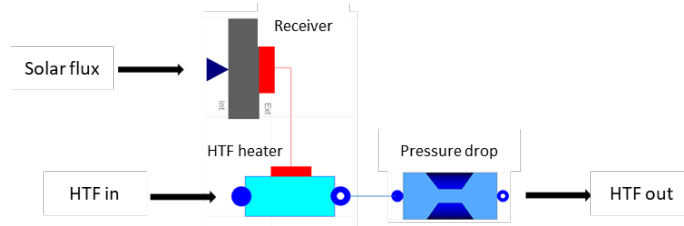
1031 - No heat loss;

1032 - Gaseous entering fluid;

1033 - Uniform temperature in the volumetric solar receiver;

1034 - Constant convective heat transfer coefficient.

1035



1036

1037

Figure A3. Schematic diagram of the volumetric solar receiver created in the Dymola environment

1038

1039

1040

The energy conservation in the solar receiver is described in Eq. (A33).

$$m_{receiver} \cdot C_p_{receiver} \cdot \frac{dT_{receiver}}{dt} = \varphi_{sol} \cdot S_{sol} \cdot C + S_{receiver/HTF} \cdot H_{receiver/HTF} \cdot (T_{receiver} - T_{HTF}) \quad (A33)$$

1041

with: - $m_{receiver}$, the mass of the solar receiver (kg)

1042

- $C_p_{receiver}$, the specific heat of the solar receiver ($J \cdot kg^{-1} \cdot K^{-1}$)

1043

- $T_{receiver}$, the receiver temperature (K)

1044

- φ_{sol} , the solar flux ($W \cdot m^{-2}$)

1045

- S_{sol} , the receiver surface area (m^2)

1046

- C , the receiver concentration ratio

1047

- $S_{receiver/HTF}$, the receiver total exchange area between the receiver wall and the HTF (m^2)

1048

- $H_{receiver/HTF}$, the heat transfer coefficient ($W \cdot m^{-2} \cdot K^{-1}$)

1049

- T_{HTF} , the HTF mean temperature (K)

1050

1051

Energy conservation for the HTF flow is written as Eq. (A34).

$$V_{HTF} \cdot \rho_{HTF} \cdot \frac{dh_{HTF}}{dt} + \dot{m}_{HTF} \cdot (h_{HTF_{out}} - h_{HTF_{in}}) = S \cdot h_{sw} \cdot (T_{wall} - T_{HTF}) \quad (A34)$$

1052

with: - V_{HTF} , the volume of the HTF (m^3)

1053

- ρ_{HTF} , the density of the HTF ($kg \cdot m^{-3}$)

1054

- h_{HTF} , the average mass enthalpy ($kJ \cdot kg^{-1}$)

1055

- \dot{m}_{HTF} , the mass flow-rate of the HTF ($kg \cdot s^{-1}$)

1056

- $h_{HTF_{out}}$, the mass enthalpy of the HTF at the outlet ($kJ \cdot kg^{-1}$)

1057

- $h_{HTF_{in}}$, the mass enthalpy of the HTF at the inlet ($kJ \cdot kg^{-1}$)

1058

1059

The heat transfer coefficient H is calculated by the Albanakis correlation [Albanakis, 2009].

$$Nu = \frac{H \cdot d_p}{\lambda} \quad (A35)$$

$$Nu = 0.76 \cdot Re^{0.4} Pr^{0.37} \text{ for } Re < 40 \quad (A36)$$

1060

with: - Nu , the Nusselt number

1061

- λ , the thermal conductivity of the metallic foam ($W \cdot m^{-1} \cdot K^{-1}$)

1062

- d_p , the average diameter of the pores (m)

1063

- Pr , the Prandtl number

1064

- Re , the Reynolds number calculated by Eq. (A37)

1065

$$Re = \frac{u_p \cdot L_c}{\nu} \quad (\text{A37})$$

1066 with - ν , the kinematic viscosity ($\text{m}^2 \cdot \text{s}^{-1}$)
1067 - u_p , the velocity in the pores ($\text{m} \cdot \text{s}^{-1}$)
1068 - L_c , the characteristic length (m), calculated by Eq. (A38) [Lu, 2006].

$$L_c = (1 - e^{-(1-\varepsilon) \cdot 0.04}) \cdot d_f \quad (\text{A38})$$

1069 with: - ε , the foam porosity ratio
1070 - d_f , the fiber's diameter (m)

1071

1072 The relation between d_f , d_p and ε can be described by Eq. (A39) [Zhao, 2001].

$$\frac{d_f}{d_p} = 1.18 \cdot \sqrt{\frac{1 - \varepsilon}{3 \cdot \pi}} \cdot \left(\frac{1}{1 - e^{-(1-\varepsilon) \cdot 0.04}} \right) \quad (\text{A39})$$

1073 with d_p , the pore average diameter (m)

1074

1075 The pressure drop ΔP in the solar receiver was calculated by the Wu correlation [Wu, 2010],
1076 shown in Eq. (A40).

$$\frac{\Delta P}{\Delta z} = \frac{1039 - 1002\varepsilon}{d_p^2} \cdot \mu_{HTF} \cdot u_p + \frac{0.5138 \cdot \varepsilon^{-5.739}}{d_p} \cdot \rho_{HTF} \cdot u_p^2 \quad (\text{A40})$$

1077 with - ΔP , the pressure drop (Pa)
1078 - Δz , the foam thickness (m)
1079 - d_p , the pore mean diameter (m)
1080 - μ_{HTF} , the HTF dynamic viscosity ($\text{m}^2 \cdot \text{s}^{-1}$)
1081 - u_p , the velocity in the pores ($\text{m} \cdot \text{s}^{-1}$)

1082

1083

1084 A3. Modeling of the heat exchanger

1085

1086 The modeling of heat exchanger is based on a fixed pinch temperature: minimum
1087 temperature difference between two fluids. Following assumptions were made.

- 1088 - Incompressible fluid
- 1089 - No heat loss
- 1090 - Fixed pinch temperature

1091

1092 The indices *in*, *out*, *pinch*, *sat* indicate the inlet, the outlet, the pinch and the saturation
1093 points; the indices *hot* and *cold* indicate the hot and the cold fluids.

1094

1095 The energy conservation in the heat exchanger between the hot and the cold fluids can be
1096 written in Eq. (A41).

$$h_{cold_{out}} = h_{cold_{in}} - \frac{\dot{m}_{hot}}{\dot{m}_{cold}} \cdot (h_{hot_{out}} - h_{hot_{in}}) \quad (A41)$$

1097 with - h , the average masse enthalpy (kJ.kg⁻¹)

1098 - \dot{m} , the mass flow-rate (kg.s⁻¹)

1099

1100 The pinch temperature ΔT_{pinch} between the hot and the cold fluids is calculated by:

$$\Delta T_{pinch} = T_{hot_{pinch}} - T_{cold_{pinch}} \quad (A42)$$

1101 with: - T , the fluid temperature (K)

1102

1103 The hot fluid mass enthalpy at pinch point ($h_{hot_{pinch}}$) is calculated with Eq. (A43):

$$h_{hot_{pinch}} = h_{hot_{in}} - \frac{\dot{m}_{cold}}{\dot{m}_{hot}} \cdot (h_{cold_{out}} - h_{cold_{sat}}) \quad (A43)$$

1104 with - h , the average mass enthalpy (kJ.kg⁻¹)

1105 - \dot{m} , the mass flow-rate (kg.s⁻¹)

1106

1107

1108 *A4. Modeling of the evaporator*

1109

1110 The modeling of the simplified evaporator is based on a fixed-by-user outlet temperature of
1111 the hot fluid. It allows a very robust operation and simplified pressure variations. The modeling
1112 assumptions are as follow:

1113 - Incompressible fluid

1114 - No heat loss

1115 - Fixed hot fluid outlet temperature

1116

1117 The indices *in*, *out* indicate the inlet, the outlet points; The indices *hot* and *cold* indicate the
1118 hot and the cold fluids.

1119

1120 The energy conservation in the evaporator between the Rankine fluid (Cold) and the HTF
1121 (Hot) can be written as Eq. (A44):

$$h_{cold_{out}} = h_{cold_{in}} - \frac{\dot{m}_{hot}}{\dot{m}_{cold}} \cdot (h_{hot_{out}} - h_{hot_{in}}) \quad (A44)$$

1122 with: - h , the fluid average mass enthalpy (kJ.kg⁻¹)

1123 - \dot{m} , the mass flow-rate (kg.s⁻¹)

1124

1125

Appendix B. Parameter values and variables fixed by the user for the dynamic simulation

Table B1. List of all PID-controllers

Phase	Target	Controlled element	Controller type	Varied parameter
1, 2	HTF's temperature at the outlet of the solar receiver	Compressor rotation speed	PI	Variation of the HTF flowrate
2	Vapor temperature at the outlet of the evaporator	Three-way valve opening/closing	PI	Variation of the HTF flowrate passing through the evaporator
3	Vapor temperature at the outlet of the evaporator	Compressor rotation speed	PI	Variation of the HTF flowrate passing through the evaporator
2,3	Pressure at the inlet of the turbine (Rankine cycle)	Turbine's partial arc variation	PI	Variation of the fluid pressure drop in the turbine
1, 2, 3	Pressure of the hot fluid in the condenser	Flow rate of cooling fluid	PI	Variation of the cooling fluid flow rate passing through the condenser
3	Pressure of the steam entering into the TCES	Withdrawal valve for the extraction from the turbine	PID	Variation of the withdrawal flow rate between high pressure and low pressure
2, 3	Tank's water level	Pump's rotation speed	PI	Variation of the water flow rate outgoing from the tank
2, 3	Fluid temperature at the outlet of the open feedwater heater	Withdrawal valve for the extraction from the turbine	PI	Variation of the withdrawal flow rate between high pressure and low pressure

1133
1134
1135

Table B2. Parameter values for different components of the system

	Parameters	Thermal Int.	Mass Int.	Turbine Int.
HTF				
	Type of fluid	Air	Air	Air
Solar Receiver	Masse (kg)	10000	10000	10000
	External surface area (m ²)	1503	1534	1396
	Internal surface area (m ²)	18000	18000	18000
	Heat transfer coefficient (W.K ⁻¹ .m ⁻²)	150	150	150
Compressor	Isentropic efficiency	0.85	0.85	0.85
	Volumetric efficiency	+	+	+
TCES Reactor	Masse of CaO (kg)	1.10×10 ⁷	1.16×10 ⁷	1.11×10 ⁷
	Length/width of CaO plate (m)	6/1	6/1	6/1
	Thickness of CaO plate (mm)	30	30	30
	Thickness of diffuser plate (mm)	5	5	5
	Thickness of wall plate (mm)	2	2	2
	Initial temperature (°C)	495	495	495
	Reaction enthalpy (J.mol ⁻¹)	104000	104000	104000
	Heat capacity ENG (J.K ⁻¹ .kg ⁻¹)	700	700	700
	Density ENG (kg.m ⁻³)	2250	2250	2250
	Rate of salt (%)	90	90	90
	Kinetic reaction coefficient	5×10 ⁻³	5×10 ⁻³	5×10 ⁻³
	Stoichiometric reaction coefficient	+	+	+
	Convective heat transfer coefficient between wall and reactive salts (W.K ⁻¹ .m ⁻²)	400	400	400
Turbine 2	Isentropic efficiency	-	-	0.85
	Volumetric efficiency	-	-	+
Pumps	Isentropic efficiency	0.85	0.85	0.85
	Volumetric efficiency	+	+	+
Turbine 1 High Pressure part	Isentropic efficiency	0.85	0.85	0.85
	Volumetric efficiency	+	+	+
Turbine 1 Low pressure part	Isentropic efficiency	0.85	0.85	0.85
	Volumetric efficiency	+	+	+
Evaporator	HTF outlet temperature (°C)	250	250	250
Condenser	Volume (m ³)	100	100	100
	Cold fluid exit temperature (°C)	30	30	30
	Incondensable partial pressure (bar)	0	0	0
Evaporator bleeding	Pinch point (°C)	10	10	10
	Incondensable partial pressure (bar)	0	0	0
	Volume (m ³)	10	10	10
Heat exchanger 1	Pinch point (°C)	10	10	-

1136
1137

1138
1139

Table B3. Variables fixed by user—Phase 1

	Parameters	Thermal Int.	Mass Int.	Turbine Int.
HTF				
	HTF-pressure (bar)	15	15	15
Solar receiver	HTF exit temperature (°C)	600	600	600
TCES reactor				
	Steam exit pressure (bar)	+	+	+
Turbine 2				
	Turbine exit pressure (bar)	-	-	0.08

1140
1141
1142
1143

Table B4. Variables fixed by user—Phase 2

	Parameters	Thermal Int.	Mass Int.	Turbine Int.
HTF				
	HTF pressure (bar)	15	15	15
Solar Receiver	HTF outlet temperature (°C)	600	600	600
TCES Reactor				
	Steam outlet pressure (bar)	+	+	+
Turbine 2				
	Turbine outlet pressure (bar)	-	-	0.08
Pumps				
	Evaporator inlet pressure (bar)	80	80	80
Open feedwater heater				
	Pressure (bar)	8	8	8
	Temperature (°C)	42	42	160
Turbine 1 High Pressure part				
	Inlet pressure (bar)	80	80	80
	Outlet pressure (bar)	8	8	8
Turbine 1 Low Pressure part				
	Inlet pressure (bar)	8	8	8
	Outlet pressure (bar)	0.08	0.08	0.08
Evaporator				
	Rankine fluid exit temperature (°C)	480	480	480
Condenser				
	Vapor pressure (bar)	0.08	0.08	0.08
	Liquid level	0.6	0.6	0.6

1144
1145
1146

Table B5. Variables fixed by user—Phase 3

	Parameters	Thermal Int.	Mass Int.	Turbine Int.
HTF				
	HTF pressure (bar)	15	15	15
TCES Reactor				
	Steam inlet pressure (bar)	+	+	+
	Steam state	Saturated	Saturated	Saturated
Pumps				
	Evaporator enter pressure (bar)	80	80	80
Open feedwater heater				
	Pressure (bar)	8	8	8
	Temperature (°C)	42	42	160
Turbine 1 High Pressure Part				
	Inlet pressure (bar)	80	80	80
	Outlet pressure (bar)	8	8	8
Turbine 1 Low Pressure Part				
	Inlet pressure (bar)	8	8	8
	Outlet pressure (bar)	0.08	0.08	0.08
Evaporator				
	Rankine fluid outlet temperature (°C)	480	480	480
Condenser				
	Vapor pressure (bar)	0.08	0.08	0.08
	Liquid level	0.6	0.6	0.6
	Incondensable partial pressure (bar)	0	0	0
Heat exchanger 2				
	Inside pressure (bar)	+	+	+
	Liquid level	0.6	0.6	0.6

1147